Doctoral Thesis

博士論文

Characterization of laser-induced discharge extending in various gas species

(様々なガス種中を進展するレーザー誘起放電の研究)

オフォス　ジョセフ　アンペドゥ

(Ofosu Joseph Ampadu)

東京大学 大学院新領域創成科学研究科

基盤科学研究系

先端エネルギー工学専攻

平成３０年度

博士論文

Characterization of laser-induced discharge extending in various gas species

(様々なガス種中を進展するレーザー誘起放電の研究)

2018 年 3 月提出

指導教員　小紫　公也　教授

47-147017　Ofosu Joseph Ampadu

Graduate School of Frontier Sciences, The University of Tokyo

Transdisciplinary Sciences, Department of Advanced Energy

2017-2018

Doctoral Thesis

Characterization of laser-induced discharge extending in various gas species

Submitted March 2018

Supervisor: Professor Komurasaki Kimiya

47-147017 Ofosu Joseph Ampadu

SUMMARY

Repetitively pulsed (RP) laser propulsion, is one of the concepts of beamed energy propulsion, which has the potential of placing kilograms of payload mass fraction into earth orbits. RP propulsion systems have the capability of increased multiple missions for a given time frame due to the utilization of an off-board reusable energy source (such as a laser-based launch equipment) located either on earth or in space. Compared to conventional chemical rocket systems, laser-induced plasma discharges for propulsive applications have high specific impulse and thrust, low lift-off weight, as well as being comparatively inexpensive

Laser supported detonation (LSD) is a propagation regime in which a laser-induced plasma discharge interacting with an incident laser beam, absorbs the beam energy and efficiently propagates an ionization wave capable of inducing thrust. LSD is an over-driven detonation in which the laser-induced discharge (LID) drives a shock wave. Transition of the LSD regime to a laser supported combustion (LSC) regime occurs when the intensity of the pulsed laser decays below a required threshold. In the LSC regime, the driven shock wave propagates adiabatically and results in inefficient transfer of energy for propulsion. Therefore, understanding the Physics of laser absorption and the energy conversion processes of an LID wave is necessary to design and develop efficient laser-propelled thrusters.

The objectives of the study were given as first, experimentally demonstrate in various gases, that the LID propagation in sufficiently large effective beam diameter D, can uniquely define the LID extension velocity U_{LID}, as a function of the laser intensity S;

$U_{\mathrm{LID}} \propto S^{\alpha}$, as well as obtain the exponential parameter α for various gases. The second was to evaluate and validate a 1-D LID photoionization model proposed by Shimamura, by comparing analytical results to that of experiment.

U_{LID} was measured in helium and argon gases using laser shadowgraph technique, with a CO_2 gas laser as the source for discharge induction. The dependence of U_{LID} on gas species and laser beam diameters were ascertained. A threshold value of the beam diameter, was necessary to uniquely define the relation $U_{\mathrm{LID}} \propto S^{\alpha}$. The D sufficiently large to uniquely define the relation $U_{\mathrm{LID}} \propto S^{\alpha}$ and to eliminate lateral dissipation of energy was 7.2 mm in all the gases studied. Moreover, the slopes of the relation (α) were different from that of Chapman-Jouguet detonation theory. The slopes were 1.18, 0.46 and 0.23 respectively, for helium, air and argon gases. These differences would be a key to understanding the physics of LID. The differences validate the hypothesis of this study that the LID propagation is a discharge-based phenomenon. Thus, the extension velocity U_{LID}, should be determined from discharge-based physics and not fluid dynamics.

U_{LID} was analytically obtained using Shimamura's 1-D LID photoionization model with experimentally obtained propagation properties of the induced discharge as input. The objective was to evaluate and validate the model by comparing analytically obtained results to that of experiment. The electron number density and excitation temperature of the bulk plasma were obtained from optical emission spectroscopy experiment. The spectra obtained for the argon gas could not be classified as either from an optically thick or thin plasma. Thus, the measured properties of argon gas were not used for the validation of the model. The 1-D LID model could reproduce the increasing slope tendency of U_{LID} as a function of S in helium plasma. However, the absolute values of U_{LID} were 300% - 600% overestimated. This is because of the 100% utilization of

absorbed energy for ionization assumed in the model. The model does not consider the consumption of absorbed energy for excitation of neutral particles.

The percent values of absorbed energy used for ionization was obtained to be 5% - 25% as a function of intensity for the LID helium plasma. Less energy was consumed for ionization in low intensity region compared to high intensity region. This observation contradicts the 100% utilisation of absorbed energy for ionization in the Shimamura's 1-D LID model. Based on the obtained results, the study concluded that higher excitation energies are necessary to sustain the induced discharge, especially in the low intensity region. In order to improve the model, a two-step ionization process accounting for fractions of absorbed energy was proposed to be incorporated in to the 1-D LID model. This involves energy storage in neutral particles' excitation mode and subsequent ionization via collisions of excited neutrals with field-accelerated electrons.

ACKNOWLEDGEMENT

I am first and foremost thankful to the Lord God Almighty, who has been merciful and gracious unto me.

My utmost and heartfelt gratitude goes to my wonderful wife Keiko, for her understanding and love towards me. I am thankful to my son Yusei, for allowing me stay away from him during the final period of preparations and completion.

I would like to express my profound gratitude to my supervisor, Professor Kimiya Komurasaki for his advice, education, counsel and all the academic guidance and exposures he granted me. I would also like to thank Professor Hiroyuki Koizumi, for his advice granted me during my entire graduate program at the University of Tokyo. I am thankful to Assistant Professor Rei Kawashima for the guidance on numerical coding and analysis. I am thankful to Mr. Kohei Matsui, my colleague on the Laser Propulsion team for his support on this work. Thanks to all members of the Komurasaki & Koizumi laboratory, past and present, of both the Advanced Energy and Aeronautics & Astronautics departments, who made my stay in Japan an enjoyable one. I am sincerely grateful.

I also appreciate my parents, Mr. Paul and Mrs. Janet Ampadu for their forthcoming advice every time I ran to them. I am also thankful to my siblings and my family in Ghana I am very thankful to my brother Mr. Stephen K. B Omane and my friend Mr. Alex Twumasi Boakye for their encouragement, support and counsel towards me all these years.

I am thankful to the Ministry of Education, Culture, Sports, Science and Technology (MEXT [MONBUKAGAKUSHO]) for the scholarship award for the first three years (2014-2017) of my doctoral degree program. I am also thankful to the Atsumi International Scholarship Foundation for the scholarship granted me during the final year (2017-2018) of this study.

I am thankful to Pastor Peter Okada and Mrs. Hideko Okada of the Tokyo Baptist Church, Misato Campus, for their love and advice.

I am also thankful to all my loved ones and friends who assisted me in diverse ways. Especially, my core friends in Japan who stick closer like brothers. These are Emmanuel Apiors, Gideon Baffoe, James Ochieng and Christian Uduije. Thank you guys, you have been a wonderful family.

Ofosu Joseph Ampadu

March 23, 2018.

TABLE OF CONTENTS

LIST OF TABLES

LIST OF FIGURES

NOMENCLATURE

A	ion broadening parameter/ temperature function
B_λ	Spectral intensity per unit wavelength, Wm^{-3}
c	speed of light in vacuum, ms^{-1}
D	plasma diameter, m
D	effective laser beam diameter, mm
D_e	electron diffusion coefficient, m^2s^{-1}
d	thickness of radiating layer, m
E	energy, eV (J) / electric field, Vm^{-1}
E_exc	absorbed energy for excitation, J/kg
E_i	absorbed energy for ionization, J/kg
e	electron charge magnitude, C
G	Gaunt factor
g	statistical weight
h	Planck constant, Js
I_sp	specific impulse, s
J	radiation intensity per unit solid angle, $W.m^{-2}.sr^{-1}$
j_i	volumetric radiation density, Wm^{-3}
j_λ	volumetric radiation per unit wavelength, Jm^{-4}
j_ν	volumetric radiation per unit frequency, Jm^{-3}
k_B	Boltzmann constant, J/K
k_IB	IB absorption coefficient, m^{-1}
k_re	recombination coefficient, m^6s^{-1}
L	plasma absorption thickness, m
l	absorption length, m
l_IB	IB absorption length, m
M^2	laser beam quality factor
m_e	electron mass, kg

n_{e}	electron number density, m^{-3}
n_{i}	ion number density, m^{-3}
n_{n}	neutral number density, m^{-3}
$n_{\mathrm{e,f}}$	precursor/ front electron number density, m^{-3}
$n_{\mathrm{e,peak}}$	peak electron number density, m^{-3}
Q	momentum transfer cross section, cm^2
R	Debye shielding parameter
r	radius of radiating layer, m
S	laser intensity, Wm^{-2} / source term
T_{e}	electron temperature, eV (K)
T_{ex}	electron excitation temperature, eV (K)
t	time, s
U_{CJ}	C-J detonation velocity, ms^{-1}
U_{est}	estimated LID extension velocity, ms^{-1}
U_{LID}	LID extension velocity, ms^{-1}
U_{R}	estimated LID extension velocity with recombination, ms^{-1}
u_{e}	electron drift velocity, ms^{-1}
w_{e}	electron impact width
w_{t}	full-width at half-maximum, nm
x	displacement, m
Z_{eff}	effective nuclear charge
α	exponential parameter
α_{IB}	IB absorption coefficient, m^2
γ	ratio of specific heats
ΔE_{i}	fraction of absorbed energy used for ionization, J/kg
Δh	change in enthalpy, J/kg
ε_o	permittivity of free space, Fm^{-1}
ϵ_{i}	ionization potential, eV
θ	angle, radian
λ	laser wavelength, m
$\lambda_{\mathrm{mfp,pa}}$	mean free path of photon-absorption, m
$\lambda_{\mathrm{mfp,e}}$	mean free path of electron collisions, m

ν	frequency, s^{-1}
ν_c	cut-off frequency, s^{-1}
ν_{eff}	effective ionization frequency, s^{-1}
ν_i	ionization frequency, s^{-1}
ν_m	mechanical collision frequency, s^{-1}
ρ	gas density, kgm^{-3}
τ_d	tail decay constant of CO_2 laser
ϕ	photon flux, $m^{-2}s^{-1}$
ω	laser frequency, s^{-1}

Subscripts

c	cut-off
e	electron particle
en	electron-neutral interaction
ei	electron-ion interaction
i	ion particle
0, n	neutral particle
G	Gaussian distribution
T	Top-hat distribution

LIST OF ABBREVIATIONS

BEP	Beamed Energy Propulsion
CJ	Chapman-Jouguet
CW	Continuous Wave
CFD	Computational Fluid Dynamics
DPSS	Diode Pumped Solid-State
FIW	Fast Ionization Wave
GEO	Geosynchronous Earth Orbit
GTO	Geostationary Transfer Orbit
IB	Inverse Bremsstrahlung
ICCD	Intensified Charge Coupled Device
LEO	Low Earth Orbit
LID	Laser-Induced Discharge
LIP	Laser-Induced Plasma
LITA	Laser-in-Tube Accelerator
LSC	Laser Supported Combustion
LSD	Laser Supported Detonation
LSP	Laser Sustained Plasma
LSRW	Laser-Supported Radiation Wave
PDE	Pulse Detonation Engine
RP	Repetitively Pulsed
TEA	Transversely Excited Atmospheric
UV	Ultra-Violet
ZND	Zel’dovich-Neumann-Doring

CHAPTER 1

INTRODUCTION

1.1 Beamed Energy Propulsion Overview

Beamed energy propulsion (BEP) is a propulsion concept in which collimated electromagnetic wave beam is used as a source of energy to propel a thruster. Currently, chemical rocket systems are the reliable and dependable way of accessing outer space in spite of their expensiveness. Launch costs of conventional chemical rocket systems range from approximately $5,000 per kilogram for low earth orbit (LEO), approximately $15,000 per kilogram for geostationary transfer orbit (GTO)[1] and up to about $30,000 per kilogram for geosynchronous earth orbit (GEO), depending on its orbital inclination.[2] It is quite interesting to note that the CEO of SpaceX stated that: “If one can figure out how to effectively reuse rockets just like airplanes, the cost of access to space will be reduced by as much as a factor of a hundred.”.[3] However, making the rockets reusable significantly affects its payload performance. For instance, according to SpaceX, a reusable version of their Falcon 9 rocket can lift 50 percent less payload of the fully expendable version, whiles the reusable version of their Falcon Heavy rocket can only do about 2.8 times less the payload of the expendable version.[4] This limitation on payload, even for the reusable versions of the current rocket systems is of grave concern and has significant restrictions on future space access for various missions.

Making use of systems that do not require an on-board energy source is one potential way to solve the high cost and payload limitations of current rocket systems. In this regard, BEP is one of the plausible ways, in which the energy source (laser/ microwave) could

be located either on earth or at a station in space. Another proposed system is the mass driver method, where high projectile acceleration is achieved via the application of electromagnetic force.[5-6] BEP has the potential of placing kilograms of payload mass fractions into earth orbits and the capability of increasing multiple missions for a given time frame due to the utilization of an off-board reusable source. Recent technological advances towards the development of high power oscillators for both lasers and microwaves make launch applications feasible. Moreover, the technological advances in beam pointing, tracking and focusing would be necessary for reaching targeted orbits.

A photon propulsion concept was first introduced by Sanger in 1953.[7] The first microwave concept was introduced by Shad and Moriarty in 1965.[8] In 1972, Arthur Kantrowitz was the first to propose a laser propulsion concept powered by a high-power ground-based laser.[9] Michael Minovich in that same year, proposed an in-space laser propulsion concept utilizing a remote power station.[10] In this study, repetitively pulsed (RP)[11] laser propulsion is the concept of BEP considered.

1.2 Laser Propulsion and Detonation System

Based on the physics of thrust generation, BEP concept devices are categorized as:

i. Heat exchanger thrusters

ii. Detonation thrusters (plasma formation via breakdown of ambient gas)

iii. Ablative thrusters

iv. Photonic laser thrusters.[12]

Based on the transmission mode, laser propulsion is categorized as continuous wave (CW) or repetitively pulsed (RP). In CW laser propulsion, the laser-induced discharge plasma termed as laser sustained plasma (LSP) is confined and maintained by the inverse bremsstrahlung (IB) process. This process heats the propellant gas to a higher temperature resulting in a relatively higher specific impulse I_{sp} than that of chemical rocket systems.

CW laser propulsion is considered to be a candidate for in-space propulsion since the current power levels of this device in the several kW rating, is insufficient for ground-to-space launch applications. In RP laser propulsion, pulsed laser irradiation ablates the surface of a target, termed as laser ablation, or focused laser beam breaks down an ambient gas to produce plasma. This process of plasma formation is termed as laser-induced plasma (LIP). In contrast to CW, RP laser propulsion is a suitable candidate for ground-to-space launch applications due to its MW class rating. This is because, the high temperature plasma formed by RP laser systems has the potential to increase the generated thrust. The concepts of highway of light and beam riding when successfully implemented would make long distance tracking and beam pointing to vehicles unnecessary.[13] More so, Claude Phipps proposed that laser microthrusters whose on-board diode lasers are supplied power from an array of solar panels, are a candidate for precise orbital positioning and attitude control of satellites.[14] Different forms (depending on the shape of the thruster) of propelled devices have been proposed and experimented with. These include the flat plate, pulsejet[15] and the laser in-tube accelerator (LITA).[16] Laser propulsion concept is a potential resource saving alternative with cost minimisation and low emission advantages. Very high I_{sp} and thrust are attainable in an air-breathing flight mode within the earth's atmosphere due to the elimination of mass penalty of carrying an on-board energy source.[17] This gives the vehicle a low lift-off weight.[18] The RP laser detonation thruster working gas is laser heated rather than combusted. Thus, it is a pulse detonation engine (PDE) without heavier equipment such as combustion chamber or turbo-pump systems; making the vehicle structure simple and relatively cheaper. It is important to emphasise that the laser equipment which is expected to be much more expensive than the launch cost is easily accessible, maintainable and replaceable as it is located either here on earth or in a space-based station. The proof of

the laser propulsion concept has been demonstrated by the laser Lightcraft: a typical detonation thruster.[19] It is projected that it is feasible for the laser propulsion vehicle to reach GEO without parking in LEO.[20] Brandstein and Levy showed that a 100 kg class satellite could be placed into GEO orbit with a 100 MW class laser power delivering kJ output levels per pulse.[21]

The conceptual design of the RP laser detonation thruster is as shown in Figure 1.1; typical examples are the bell nozzle type and the Lightcraft. The PDE cycle of the laser thruster is described pictorially in Figure 1.2 and as follows. A laser beam of typical wavelength and pulse width of ~μm and ~μs respectively is focused inside the bottom of the thruster to induce a discharge wave. The discharge wave generates a blast wave whose reflection off the inner wall of the thruster imparts thrust to the vehicle (Impulse generation). Refilling of gas takes place when the ambient pressure within the thruster is much lesser than the atmospheric condition, and the cycle is repeated. Katsurayama et. al. proposed three modes of flight operation, namely: pulsejet mode (within an altitude range of 0 ~ 7 km), ramjet mode (within an altitude range of 7 ~ 40 km) and the rocket mode (beyond 40 km). In the rocket mode, an on-board propellant would be necessary for thrust generation.

1.3 Laser Supported Detonation and Induced Discharge

A detonation wave is a supersonic propagating wave across which state properties such as density, pressure and temperature change or increase rapidly, and it is predominantly followed by an energy release across the wave. When a focused laser beam's intensity exceeds the breakdown threshold for the ambient gas, breakdown of the gas occurs leading to the formation of plasma (laser-induced plasma).

The laser-induced breakdown of the ambient working gas is possible with a laser intensity S, ranging from $10^{14} \sim 10^{15}$ W/m^2.[22]

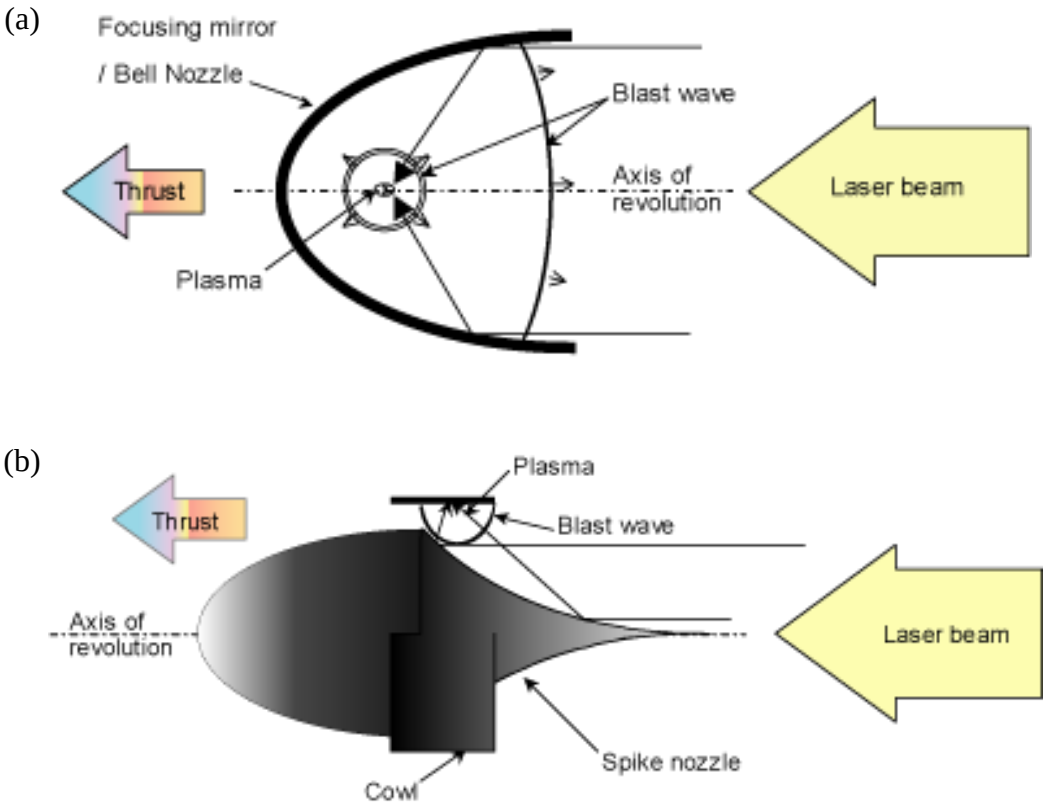

Figure 1.1 Conceptual design of RP laser detonation thruster: (a) Bell nozzle type, (b) Spike nozzle type (typical example is the Lightcraft).

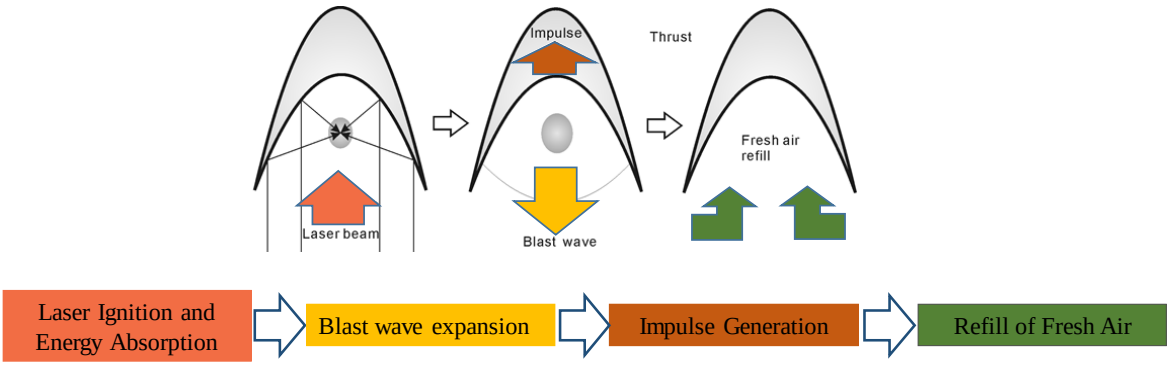

Figure 1.2 Pictorial description of PDE cycle of the laser detonation thruster.

However, this value is reducible to about 3 orders of magnitude less when the breakdown is induced at about 1 ~ 2 mm above a metal target plate.

Laser supported detonation (LSD) is a propagation regime in which a laser-induced plasma discharge, interacting with an irradiating incident laser beam, absorbs the beam energy and efficiently drives an ionization wave with the potential to induce thrust. In

this regime the induced plasma is heated isometrically.[23] The conservation of mass necessitates the requirement for the existence of a supporting piston action or an expansion wave behind the LSD. However, the LSD is a propagating wave without the piston mechanism (freely propagating detonation). Thus, the LSD is a weak[24] over-driven detonation in which the laser-induced discharge (LID) drives a shock wave. When the intensity of the pulsed laser decays below a required threshold, the LSD regime transitions into a laser supported combustion (LSC) regime. In the LSC regime, the driven shock wave propagates with an isobaric condition which results in an inefficient transfer of energy for propulsion. It is therefore important to understand the physics of laser absorption and the energy conversion process of an LID wave, so as to achieve the design and development of efficient laser-propelled thrusters in the future.

The LSD which is a type of optical detonation has a different detonation wave structure compared with chemical detonation wave structure. This is illustrated diagrammatically in Figure 1.3. The wave structure of chemical detonation is defined by the ZND model due to the principal contributions from Zeldovich,[25] von Neumann[26] and Doring.[27] In the ZND model, a leading shock front compresses and heats the combustible gas. The shock front is followed by an approximate thermally neutral induction zone where excited/ radical species are generated from the shock-heated gases. The induction zone is then followed by a reaction layer where a significant amount of chemical energy is released. The propagation mechanism is thus shock-induced. It is worth mentioning that, the induction zone presents an ignition lag between the leading shock and the reaction layer in the ZND model. In the LSD wave structure, the shock and the laser-induced plasma/ discharge layer propagate together, thus eliminating the consequences of an ignition lag and enhancing the absorption of the laser energy. Moreover, the propagation mechanism

of the LSD wave structure is discharge-induced and not necessarily regulated by shock compression effect.

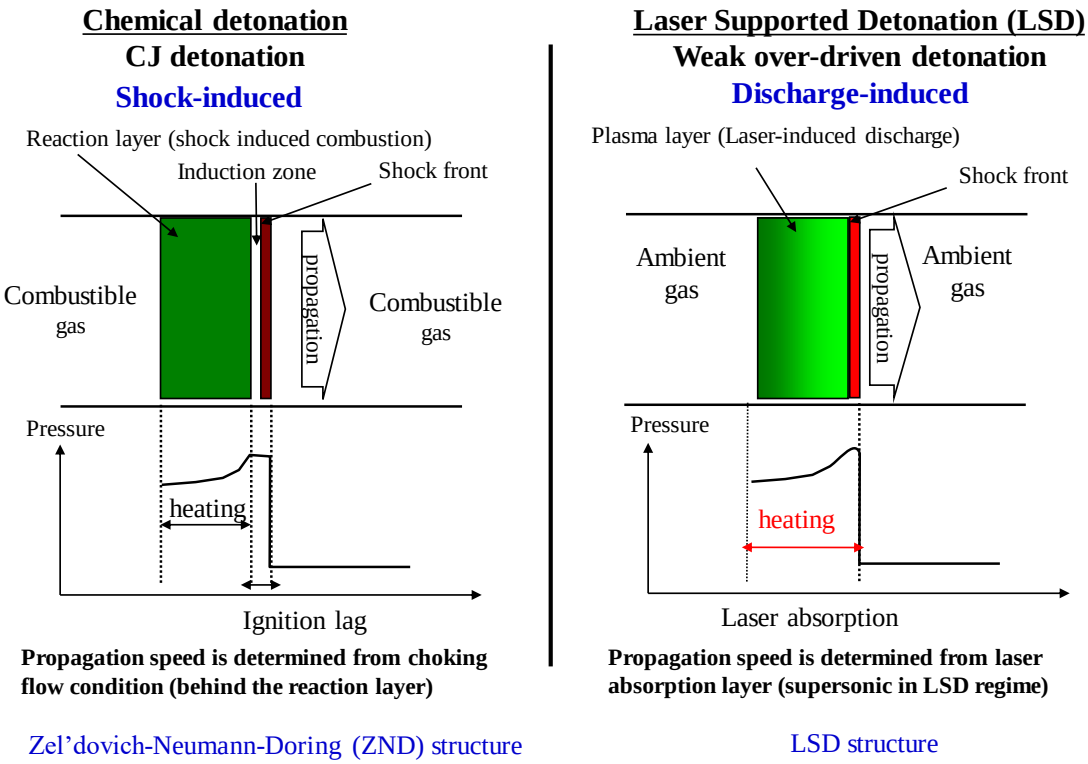

Figure 1.3 Detonation wave structure of chemical detonation and LSD.

At the threshold laser intensity S, where the LSD transitions to the LSC, the extension velocity U_{LID}, of the LID wave is defined by the Chapman-Jouguet (CJ) detonation velocity U_{CJ}. In chemical detonation theory, CJ point (shown in Figure 1.4) is determined from choking flow condition; thus U_{CJ} which is defined in Equation (1.1) has a sonic condition behind it.

$$U_{\mathrm{CJ}} = \left[2(\gamma^2 - 1)\frac{S}{\rho}\right]^{\frac{1}{3}}. \tag{1.1}$$

Where γ, S and ρ are respectively, the specific heat ratio of the ambient gas, laser intensity and gas density. Figure 1.4 show a $p - v$ diagram with a Hugoniot curve (locus of equilibrium states), Rayleigh lines (lines of constant detonation velocity) and an adiabat.[28] p and v are respectively the pressure and specific volume. The subscripts 0 and

1 represent reactant/ upstream and products/ downstream conditions respectively. Thermodynamic descriptions of the LID propagation have demonstrated that LID is weak over-driven phenomenon.[29,30] The points B (strong) and C (weak) on the diagram represent the over-driven detonation conditions. Knowledge of the detonation velocity at these points is essential for predicting and understanding the propagation condition behind the detonation wave. An accurate prediction of the extension velocity of the LID U_{LID}, is therefore necessary to define the propagation properties behind the LID for propulsive applications.

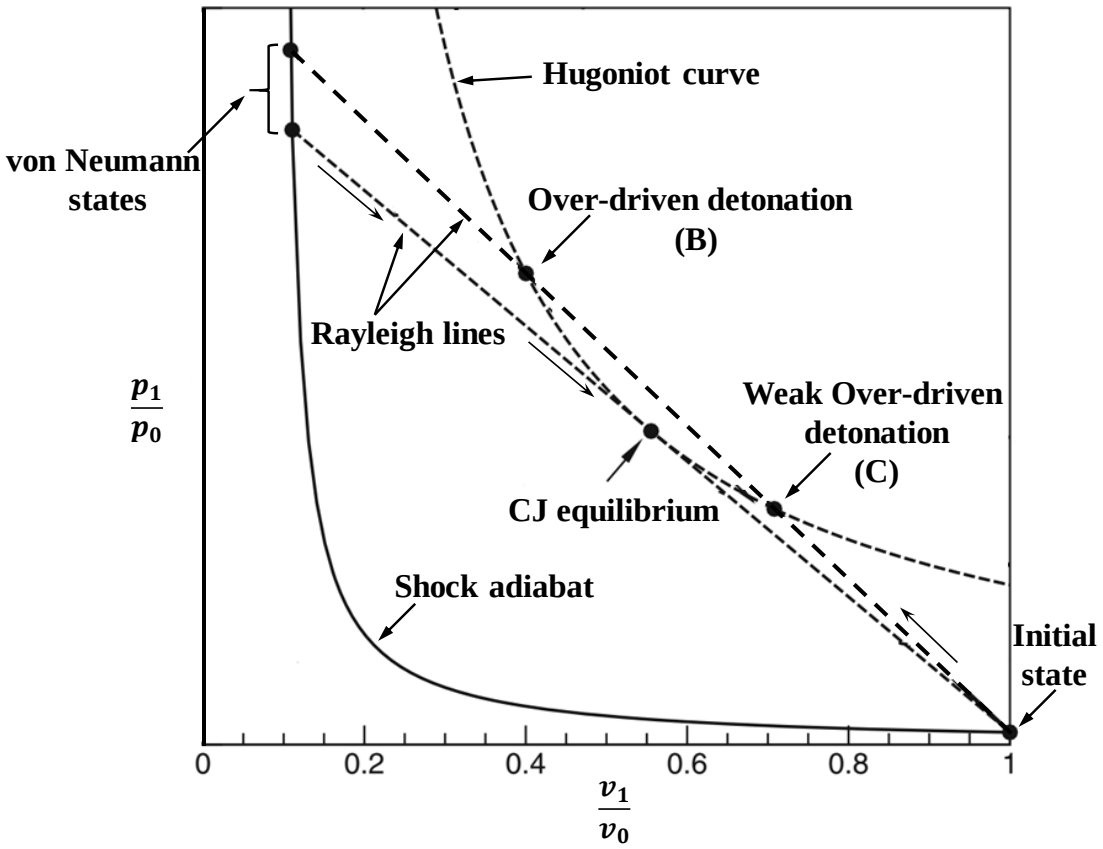

Figure 1.4 Hugoniot curves, Rayleigh lines, CJ and over-driven detonation in the $p - v$ plane.

1.4 Previous Studies

Raizer investigated the LSD termination[29] and proposed that termination occurred when the lateral expansion becomes comparable to the front propagation. The influence of the

focusing f number,[31] ambient pressure[32] and laser power density[33] on the propagation properties of the LSD wave were investigated by Mori. Raizer's lateral expansion effect[29] were investigated by Ushio *et al*.[23] Their work showed that lateral dissipation is reducible by mechanically restricting the flow in a quasi-1D space using a wedged nozzle. As a result of this restriction, the measured transition threshold laser intensity as well as the LID wave velocity were of better optimal performance characteristics for the quasi-1D confined space compared with the 2-D unconfined geometry. Shimamura *et al* studied the internal structure of the LID wave via a two-wavelength Mach-Zehnder interferometry in air.[34] Their research work revealed a non-zero electron number density n_{e} distribution at the shock front. This precursor has been also observed in streamer discharge and other related studies.[35-38] Propagation regime transition have also been investigated via Hugoniot analysis.[39]

Ramsden and Savic were one of the pioneers to introduce the term radiation-supported detonation wave.[40] They concluded per their study that, the latter phase of a laser-generated plasma, which is post LSD could be best described by Taylor's blast wave theory.[41] Raizer proposed three independent mechanisms (i.e. breakdown, hydrodynamic and radiative) for the propagation of the laser-absorption (LID) wave.[42] Raizer explained that shock-heating induced ionization and thus regulated the propagation of the LID wave. He showed that hydrodynamic and radiation mechanisms gave approximately same propagation velocities and concluded that due to complicated and incomplete data on the ranges of radiation, neither hydrodynamic nor radiation mechanisms were dominant.

Our studies[34,43] show that plasma propagation is a radiative-induced phenomenon and thus pre-ionization due to photo-absorption and photoionization play a significant role. The precursor (seed electrons) formed ahead of the shock front due to the (ultra-violet) UV radiation from the laser-induced plasma, influences the propagation of the LID before

the onset of shock compression effect. Therefore, it is reasonable to state that Raizer's theory of detonation (based on hydrodynamic relations) is inadequate to describe the phenomenon observed in laser produced plasmas. Thus discharge-based physics is required to explain the generation and propagation mechanism of the LID wave. The non-zero n_e distribution at the shock front could be due to two production mechanisms namely: electron diffusion and/ or photoionization effect. Considering air at atmospheric conditions as the ambient gas within which the plasma is induced, and taking into account the energy range starting from the ionization potential of oxygen molecule O_2 (12.06 eV) to about 200 eV, the mean-free path of electronic collisions $\lambda_{mfp,e}$, is on the order of $0.1 - 1.0$ μm based on the cross sections[44,45] within the energy range. For the same energy range, the mean-free path of photo-absorption $\lambda_{mfp,pa}$, is on the order of $10 - 100$ μm based on the cross section within the energy range.[46] Thus, photoionization, comparatively has a significant effect on the formation of the precursor. In order to study and understand this effect, Shimamura *et al* proposed a 1-D LID photoionization model[43] to describe the propagation mechanisms and properties of the LID wave.

1.5 Shimamura's 1-D LID Photoionization Model

The 1-D LID photoionization model defines the extension velocity of the LID U_{LID}, as a function of the ionization frequency ν_i, which is dependent on the input laser intensity S. The model's derivation concept is synonymous to that of streamer discharge physics and is deduced from the charge conservation principle. The equation for charge conservation is as shown in Equation (1.2).

$$\overbrace{\frac{\partial n_e}{\partial t}}^{\text{charge evolution}} + \overbrace{\nabla.(u_e n_e) - D_e \nabla^2 n_e}^{\text{transport}} = \overbrace{\vec{S}}^{\text{sources}} . \qquad (1.2)$$

Where u_e, D_e, and S are the electron drift velocity, electron diffusion coefficient and source term(s) respectively.

Streamer discharges are plasma channels which propagate by inducing ionization wave ahead of the streamer charged head. The streamer head has a strong self-consistent electric field that induces the ionization and sometimes photoionization could occur due to the radiation from the whole plasma volume. Streamers are triggered when the space-charge field becomes comparable to the applied field. The streamer charge processes involve:

- ✓ Electron transport and avalanche ionization
- ✓ Space-charge distortion effect of electric field
- ✓ Photoionization due to UV radiation from bulk plasma volume.

The temporal variations of laser schlieren images for streamer channels and shock waves induced by a positive pulsed corona discharge of 26 kV is shown in Figure 1.5.[47]

Equation (1.3) describes the 1-D LID photoionization model and its derivation is detailed in References 30 and 43.

$$U_{\mathrm{LID}} = \frac{\nu_i l}{\ln\left(n_{e.peak}/n_{e.f}\right)}. \tag{1.3}$$

Here $n_{e.peak}$ and $n_{e.f}$ are the electron number density respectively, at the peak and precursor locations, l is defined as the distance between the peak and precursor positions (see Figure 1.7), and it is estimated based on the inverse bremsstrahlung absorption of the source laser.

For bulk plasma conditions of a 12 Joule CO_2 laser-induced plasma ($n_e \sim 10^{24}$ m^{-3} and electron temperature $T_e \sim$ 2 eV), l is for instance, estimated to be 0.51 mm and 0.58 mm respectively, for argon and helium gases. The precursor position is defined as the point of non-zero n_e distribution ahead of the ionization (LID) wave. The peak position is

defined as the point of full absorption. The pictorial and graphical description of the model are as shown in Figures 1.6 and 1.7 respectively, with only right-propagating UV photon flux considered. The model is described by the following processes.

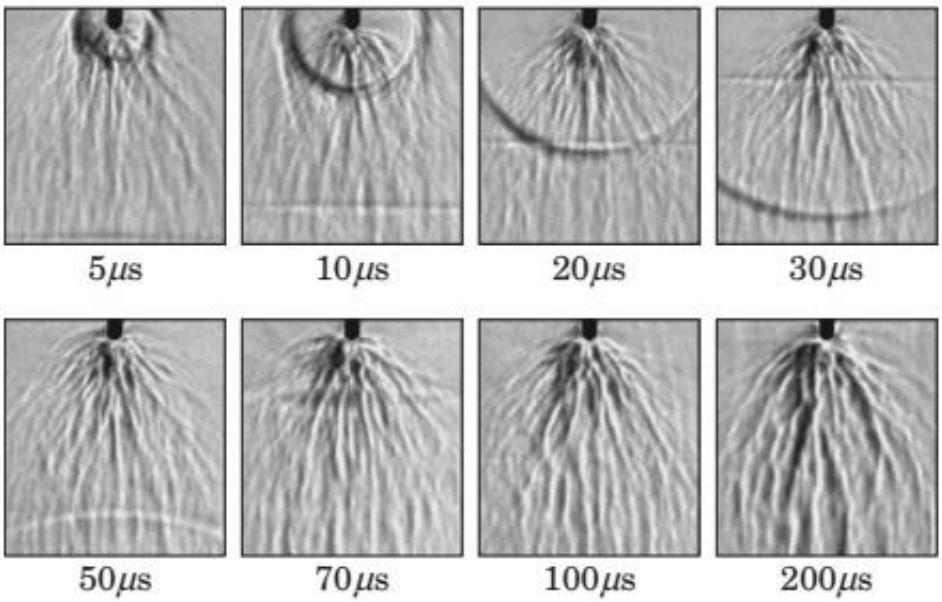

Figure 1.5 Temporal variation of laser schlieren images after the application of a 26 kV discharge pulse.[47]

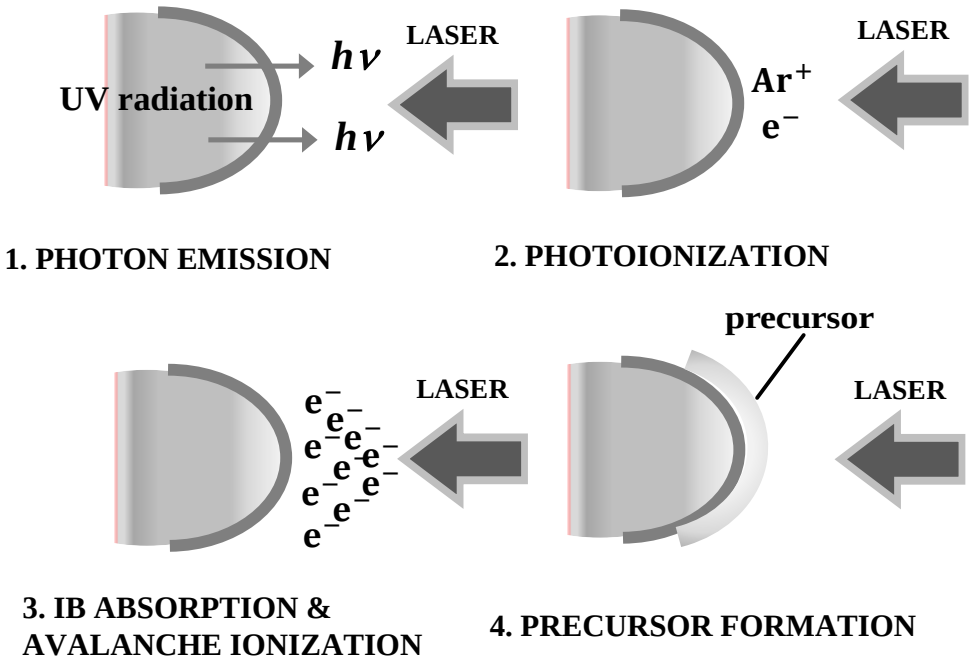

Figure 1.6 Pictorial description of the 1-D LID photoionization model.

First, the photon flux ϕ (total number of photons per unit area per second) from the bulk plasma region is absorbed by the ambient gas ahead of the ionization wave. The generation of seed electrons is the next process, and this occurs when the $h\nu$ (photon energy) of the ϕ exceeds the ionization potential of the gas.

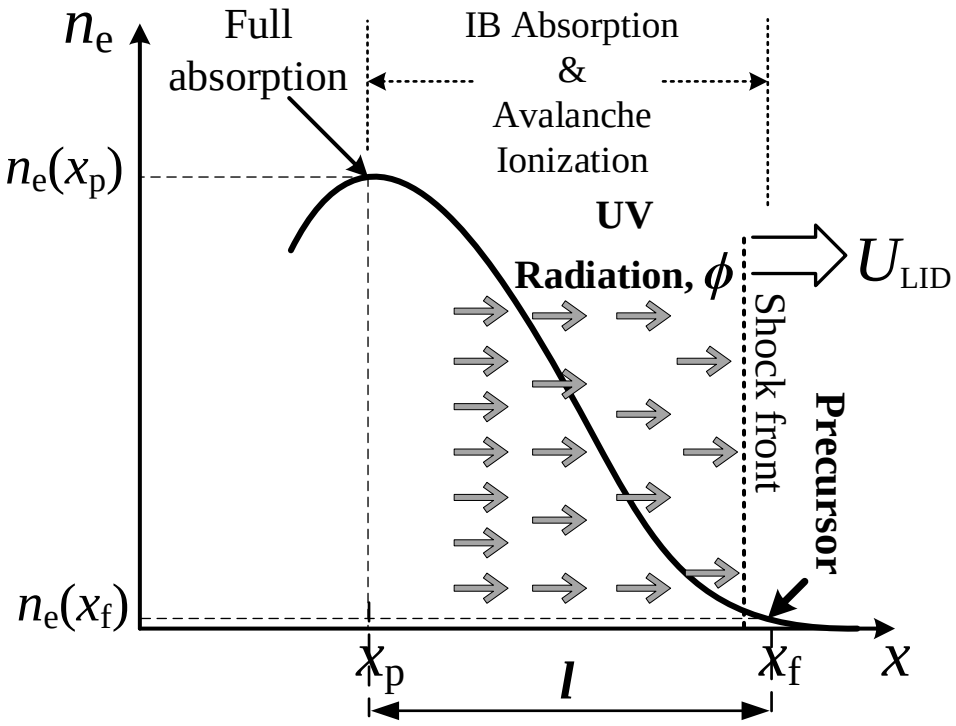

Figure 1.7 Graphical representation of the 1-D LID photoionization model.

Third, the seed electrons' interaction with the incident laser beam leads to electronic heating of particles via the inverse bremsstrahlung (IB) absorption process. This then results in avalanche ionization and the subsequent formation of the precursor.

The precursor number density distribution $n_{e.f}$, is defined as a function of ϕ and is as shown in Equation (1.4).

$$n_{e.f} = \frac{\phi}{U_{LID}} . \tag{1.4}$$

The photon flux ϕ is estimated from the total volumetric radiation (both continuum and line emissions) by integrating over frequencies with $h\nu$ above the ionization potential of the ambient working gas.

The 1-D LID model took into account only forward rate mechanism. A 3-body recombination mechanism was incorporated by redefining ν_{i} as effective ionization frequency ν_{eff} and is given in Equation (1.5).

$$\nu_{\mathrm{eff}} = \nu_{\mathrm{i}} - k_{\mathrm{re}} {n_{\mathrm{e}}}^2 \,. \tag{1.5}$$

k_{re} is the recombination coefficient.[48] A zero-dimensional analysis of the LID extension velocity was attained for the cases with and without recombination effect, U_{R} and U_{est} respectively, in argon and nitrogen gases.[49] The results revealed that recombination mechanism is quite significant. The comparisons with experimental observations are as shown in Table 1.1 and Figure 1.8 as a function of the laser intensity. The experimentally measured values were set as the per unit base values.

Table 1.1 Measured and Estimated velocities based on the model.

Parameters	**Argon**	**Nitrogen**
Measured U, kms^{-1}	1.0	1.0
Estimated U_{R}, kms^{-1}	1.17 ± 0.14	1.13 ± 0.26
Estimated U_{est}, kms^{-1}	1.50	1.52

1.1 Research Objectives

Supersonic propagation (expansion) regimes of laser-induced discharges/ plasmas are categorized or characterized based on U_{LID} as a function of S. These propagation regimes, in an order of increasing discharge velocity for a given S, are LSD wave,[29,31,50-52] laser-supported radiation wave (LSRW) and fast ionization wave (FIW).[53-56] One of the ultimate futuristic objectives of this study is the space propulsion applications of laser-induced discharges. This study therefore is limited to the LSD wave regime at which $S < 10^3$ GWm^{-2}. The reason being that, LSD wave with $S > 10^3$ GWm^{-2}, as well as LSRW and FIW regimes which are usually characterized for $S > 10^3$ GWm^{-2}, do not have substantial pressure build-up for efficient propulsive effect.

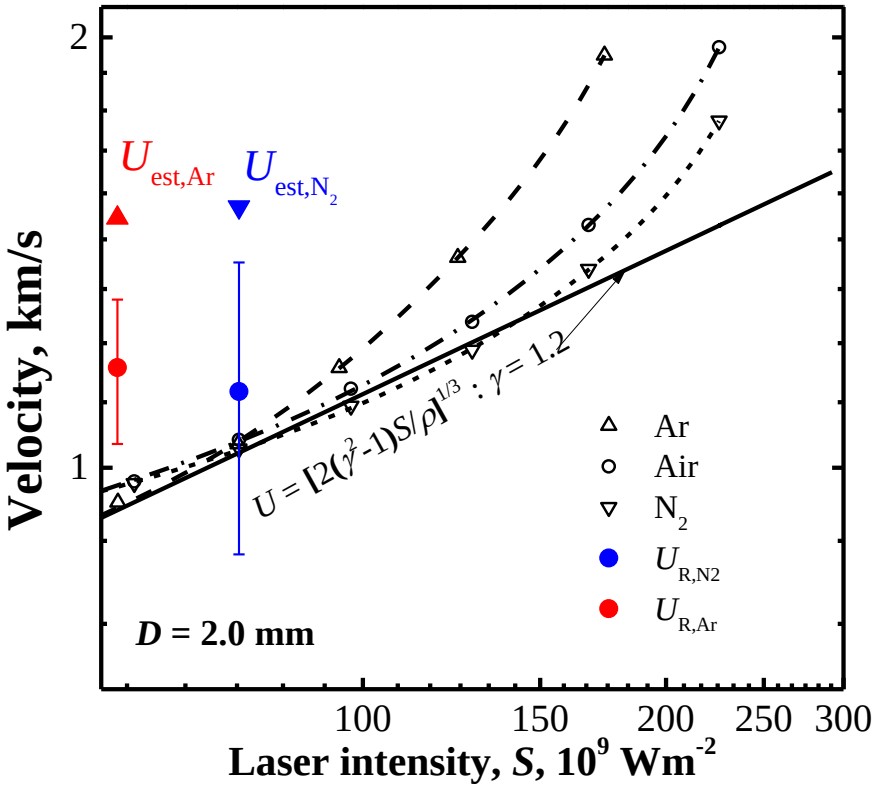

Figure 1.8 Measured and estimated LID velocities as a function of laser intensity.[49] (Effective laser beam diameter D = 2.0 mm)

Raizer predicted a power function law with an exponential value based on hydrodynamic relations, such that $U_{\mathrm{LID}} \propto S^{\alpha}$[42] and whose minimum value is defined by the Chapman-Jouguet detonation velocity U_{CJ}, for which $\alpha = 1/3$. The threshold value of the effective beam diameter at the focus D, for which U_{LID} is uniquely defined as function of the laser intensity S, was investigated by Matsui *et al*. Their experiments were conducted in atmospheric air with and without confinement of the LID wave. They concluded that a unique relation exists between U_{LID} and S when the effective diameter $D > 5.1$ mm.[57] It must be noted that, this unique relationship is independent of the input laser power or energy. Thus, the phenomenon does not depend on the propagation history and is as evidenced in Figure 1.9.

The objectives of this study were to first, investigate the influence of the ambient gas content on the extension velocity of the LID. This is because, a study of the dependence of U_{LID} on S is essential for understanding the sustenance of the LSD wave regime. The gases used were helium and argon at standard atmospheric conditions. These monoatomic gases were utilized in this study for their simple ionization kinetics which could easily be

studied both analytically and computationally. Moreover, the use of different gas species serves the purpose of identifying potential on-board propellants for the rocket mode application of laser propulsion.

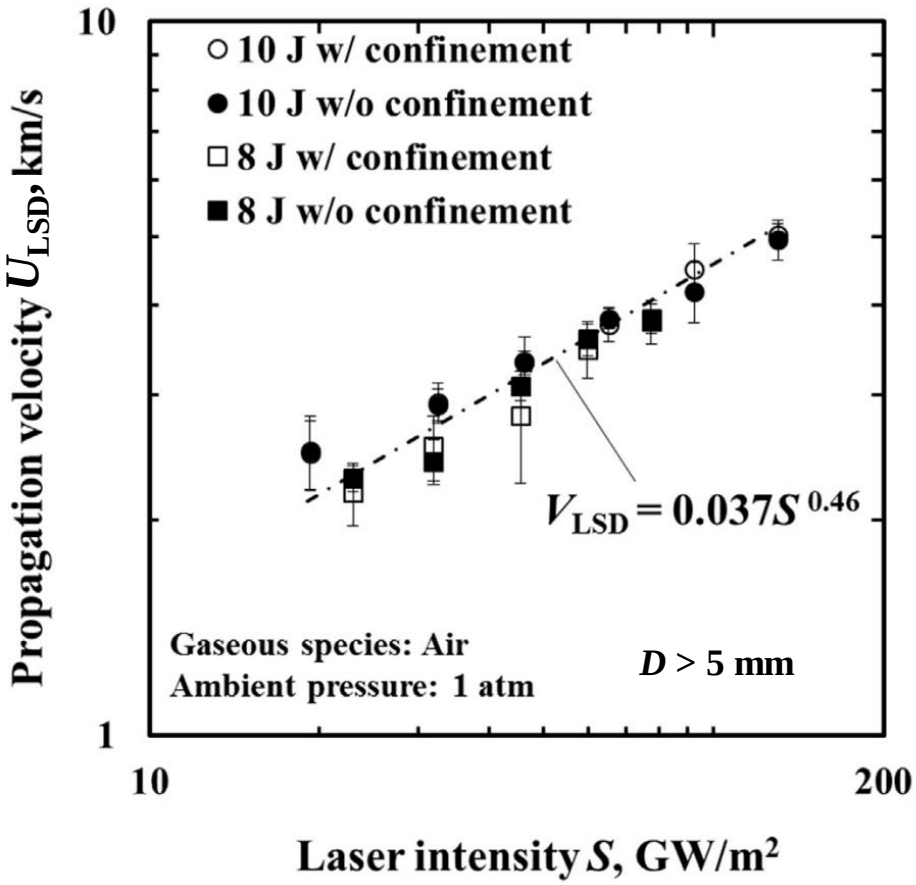

Figure 1.9 U_{LID} as a function of the laser intensity S obtained for 8 J and 10 J laser ouptuts, with and without confinement for $D > 5$ mm.[57]

Second, this study sought to accurately predict U_{LID} using Shimamura's 1-D LID photoionization model, as well as to validate the applicability of the model by comparing analytical solutions with that of experiment. This is because, a discharge model which accurately describes the propagation phenomenon, mechanisms and interactions of an induced plasma discharge is vital for the design of efficient laser-propelled thrusters in the future.

The objectives of this thesis are summarized as follows:

- ✓ Experimentally demonstrate in various gases, that LID propagation in sufficiently large D conditions can uniquely define $U_{\mathrm{LID}} \propto S^{\alpha}$, as well as obtain the parameter α for various gas species.

- ✓ Evaluate and validate the conventional 1-D LID photoionization model via comparing predicted U_{LID} by the model with measured (experimental) U_{LID}.

CHAPTER 2

MEASUREMENT OF THE LID EXTENSION VELOCITY IN ARGON AND HELIUM

2.1 Elimination of Lateral Dissipation Effect

Lateral dissipation flow could be described as the streaming out or loss of photon particles, energetic electrons and neutral particles from the induced discharge flow and results in enthalpy loss necessary for sustaining the propagation wave. The effect of this non-contributing flow was investigated by Raizer[29] who described it in terms of the ratio of the plasma absorption thickness L, to its diameter D. He investigated the transition of LSD to LSC in terms of L and D This is pictorially shown in Figure 2.1 and is described as follows. In this chapter, the discussion on the effects of L and D is extended to U_{LID}.

When L is comparable to D ($\mathrm{L/D} = 1\sim4$), lateral dissipation is significant and contextual 1-D propagation analysis is not feasible. However, when $\mathrm{L} \ll \mathrm{D}$, lateral dissipation is negligible and 1-D propagation of the induced discharge is attainable. 1-D propagation of the discharge is useful for comparison with simple analytical and numerical studies. A sufficiently large D is attainable by an array of lasers. However, for the purpose of studying the effect of lateral dissipation within the laboratory environment, large D was attained by redesigning the focusing optics of the laser beam.

Figure 2.2 shows the discharge extension velocity U_{LID}, in air as a function of the laser intensity S. The figure shows the experiment information of a point focus and a line focus of the

laser beam, whose effective beam diameters D at the focus are respectively, 1.2 mm (1.3 mm × 1.5 mm) and 0.5 mm (0.5 mm × 30 mm).[23,31].

Here we observe that U_{LID} is not uniquely defined as a function of S and thus the effective Ds were not sufficiently large enough to ensure a unique $U_{\mathrm{LID}} \propto S^{\alpha}$ relation.

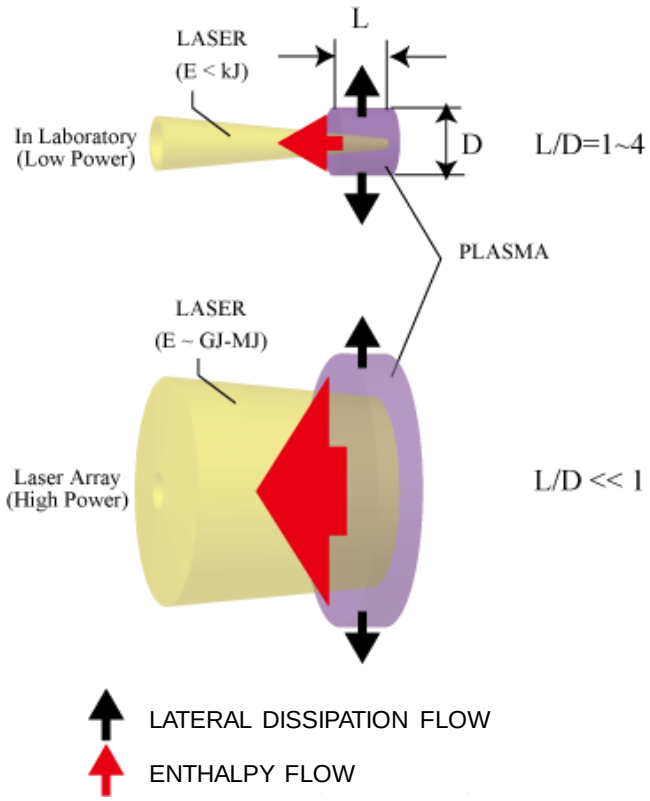

Figure 2.1 Pictorial description of lateral dissipation

Observing the data for line focusing, geometrical confinement or non-confinement had no influence on the discharge propagation velocity and thus the relation $U_{\mathrm{LID}} \propto S^{\alpha}$ is not uniquely defined. This is shown in Figure 2.3. This reasoning is corroborated by the results of Matsui *et al*[57] who conducted their study with and without geometrical confinement. They concluded that, the uniqueness of the relation $U_{\mathrm{LID}} \propto S^{\alpha}$ is dependent on a certain threshold value of D and not on confinement geometry. The threshold D in their study was 5.1 mm. Figure 2.4 shows the extension velocity U_{LID} as a function of the laser intensity S for induced discharges with $D \geq 5.1$ and $D < 5.1$ mm. Thus, the specification of a sufficiently large D is necessary for the unique definition of $U_{\mathrm{LID}} \propto S^{\alpha}$.

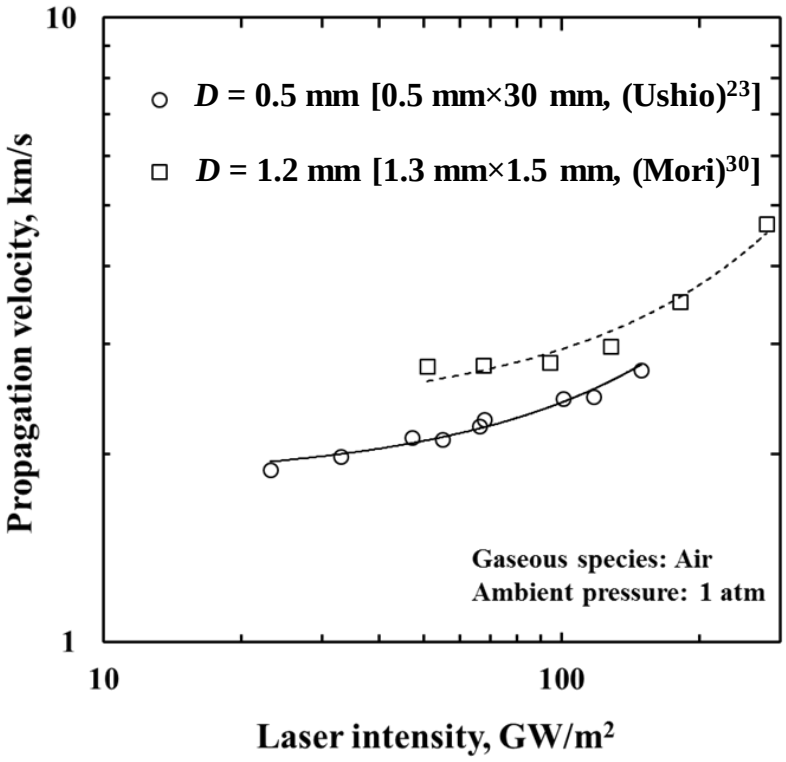

Figure 2.2 LID extension velocity as a function of S, using point focusing and line focusing laser optics.[57]

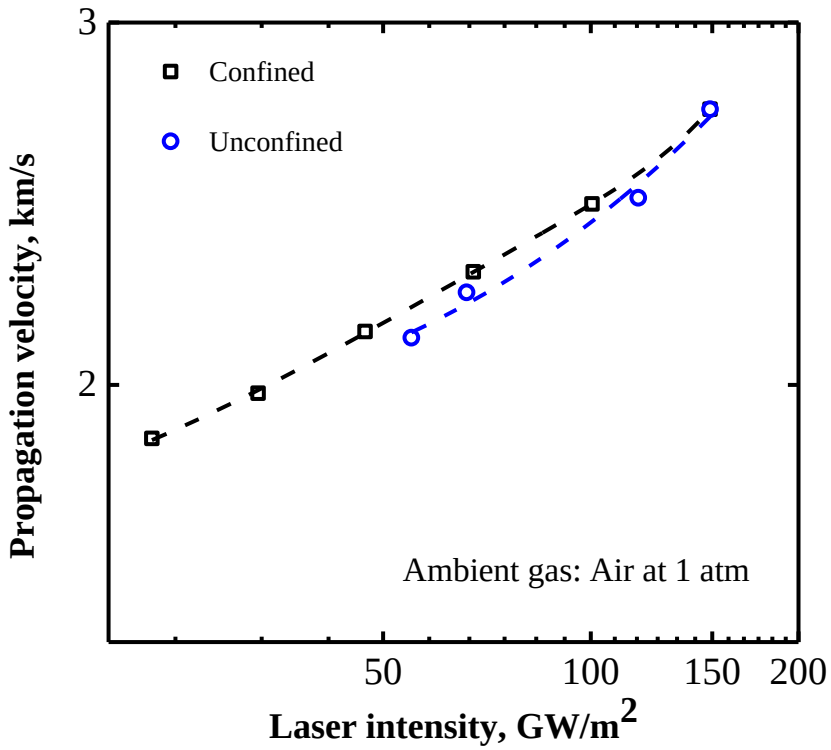

Figure 2.3 LID extension velocity as a function of S, using a line focusing laser optics with and without confinement geometry.[23]

In this study, this unique relationship and its dependence on D was investigated in argon and helium gases.

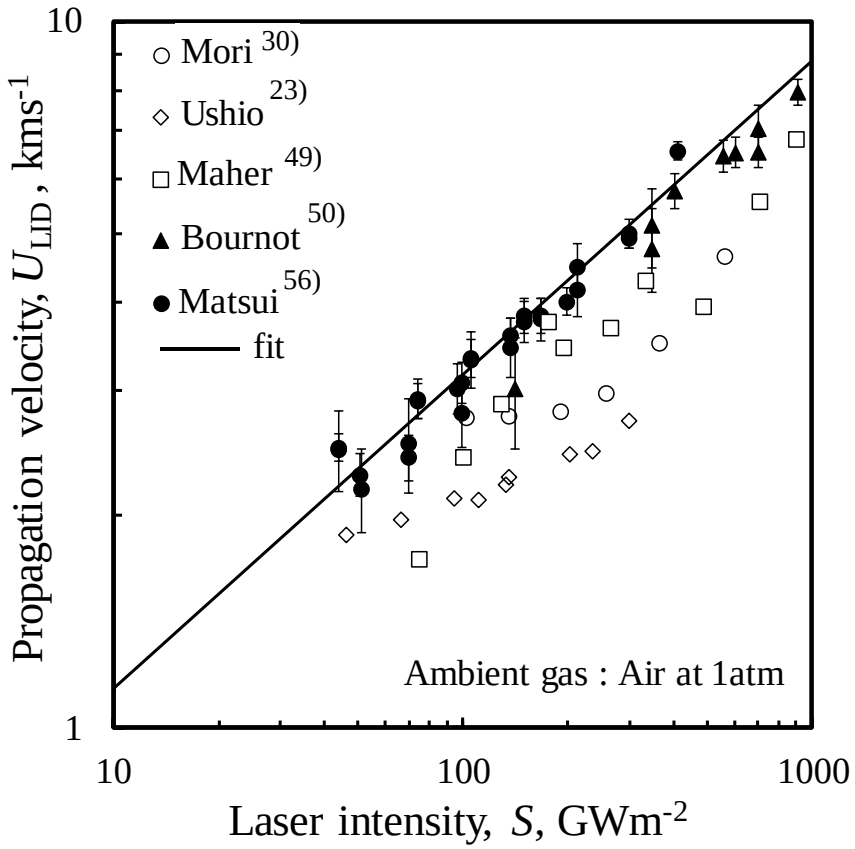

Figure 2.4 LID extension velocities U_{LID}, for induced discharges of laser optics with $D \geq 5.1$ mm and $D < 5.1$ mm. (For $D < 5.1$ mm, velocity values are below the solid fit line.)

2.2 Experimental Apparatus and Setup

In this section, the laser source and its characteristics, the focusing optics and the imaging devices are described.

2.2.1 Laser source and Focusing Optics

A transversely excited atmospheric (TEA) CO_2 pulse laser with nominal energy of 12 J was used to induce plasma for the experiments. The output energy was however, controlled within 5 J to 12 J for the purpose of avoiding multiple breakdown phenomenon. Thus, in this study, only induced discharges with single breakdown were studied. This is

due to the simplicity in studying single breakdown discharges as one whole unit interacting with the irradiated laser beam. The laser source is a product of Usho Optical System. Its beam was in the high-order multi-transverse mode. The laser beam's effective diameter D, and cross-section were 34 mm and approximately 30 × 30 mm^2 respectively. The lasing gas comprises helium, nitrogen and carbon dioxide; and has a fill pressure of approximately 120 kPa. The nominal energy increases with the fill pressure. A picture of the CO_2 laser and its specification are shown in Figure 2.5 and Table 2.1 respectively. Figure 2.6 shows the variation of the laser pulse energy with the fill pressure in the laser's discharge tube used in this study.[58] This is an increasing function of the fill pressure, representative of CO_2 gas lasers.[59,60]

Figure 2.5 Picture of the TEA CO_2 laser (exterior).

A gentec-EO joule meter (model QE50LP-H-MB) was used to measure the pulse energy before and after the experiments. The joule meter has a maximum measurable energy without attenuator of 15 J and an effective aperture size of 50 mm×50 mm. This was to ensure that the shot-to-shot pulse energy deviations were kept below ±5% throughout experiments.

Table 2.1 CO_2 laser specifications.

Model №	IRL-1201
Nominal energy	10 J
Repetition	single,0.1～0.5 Hz
Gas fill pressure	120 kPa
Output wavelength	10.6 μm
Impressed voltage	~ 10 kV
E_i fluctuation	< ± 5 %
Beam size	30 mm × 30 mm
Power source	AC100V　50／60Hz　3A
Laser gas composition	He: N_2: CO_2 = 84: 8: 8

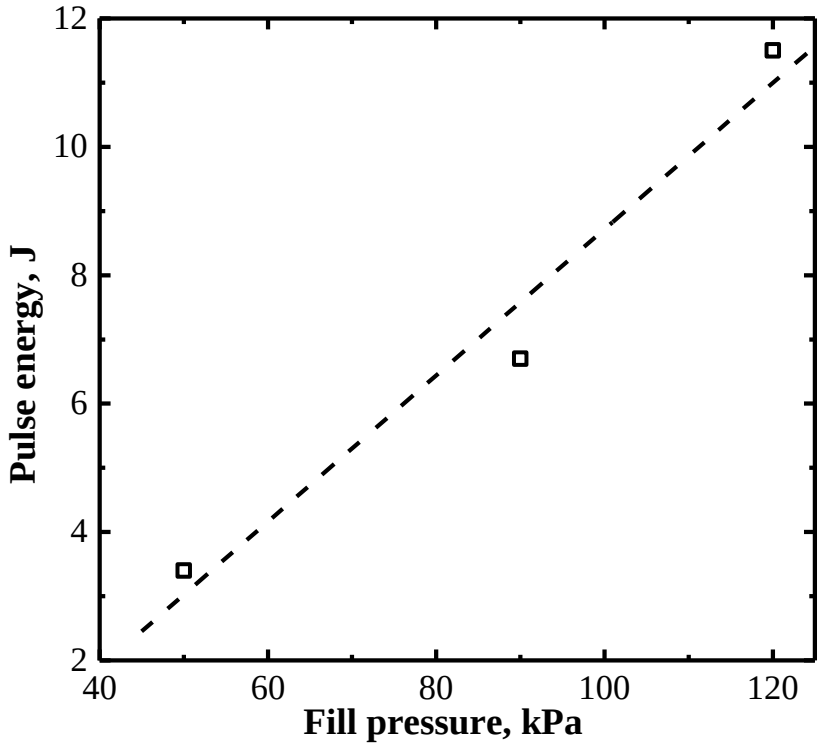

Figure 2.6 Plot of laser pulse energy versus fill pressure.

Figure 2.7 shows an image of the joule meter used in the experiments.

The pulse shape of the laser beam was detected using a photon-drag detector (Hamamatsu photonics-B749). The specification and image of the detector are shown in Table 2.2 and Figure 2.8 respectively. The laser beam's spatial intensity profile has Top-hat and

approximately Gaussian shapes in separate directions. The laser pulse has a leading-edge spike with an exponentially decaying tail, and at about 3.5 μs, 95% of the laser energy is discharged. The full width at half maximum was 0.12 ± 0.02 μs for the 10 J output case. Figure 2.9 shows the pulse shape of the CO_2 laser. The temporal change in the decaying tail power P_{tail}, can be approximately described by the following relation:

$$P_{\text{tail}} = P_{\text{o,tail}} \exp\left(-\frac{t}{\tau_{\text{d}}}\right), \tag{2.1}$$

where τ_{d} is the tail decay constant and a function of the fill pressure.

Figure 2.7 Image of the gentec-EO joule meter (model QE50LP-H-MB).

Table 2.2 Photon-drag detector specification.

Model №	B749
Aperture diameter	50 mm
Sensitivity	1.2 V/MW
Rise time (10 ~ 90%)	< 1 ns

The laser beam was focused by two distinct sets (each set is a pair) of off-axis gold-coated cylindrical mirrors and an anti-reflection (AR) coated Zinc-Selenide (Zn-Se) convex lens, in order to respectively achieve effective beam diameters D, of 9.1, 7.2 and 5.1 mm. The

gold-coated mirrors have an average reflection value of 98% whiles the AR coated Zn-Se has an average transmission value of approximately 97%. The laser beam was

Figure 2.8 Image of the photon-drag detector (Hamamatsu photonics-B749).

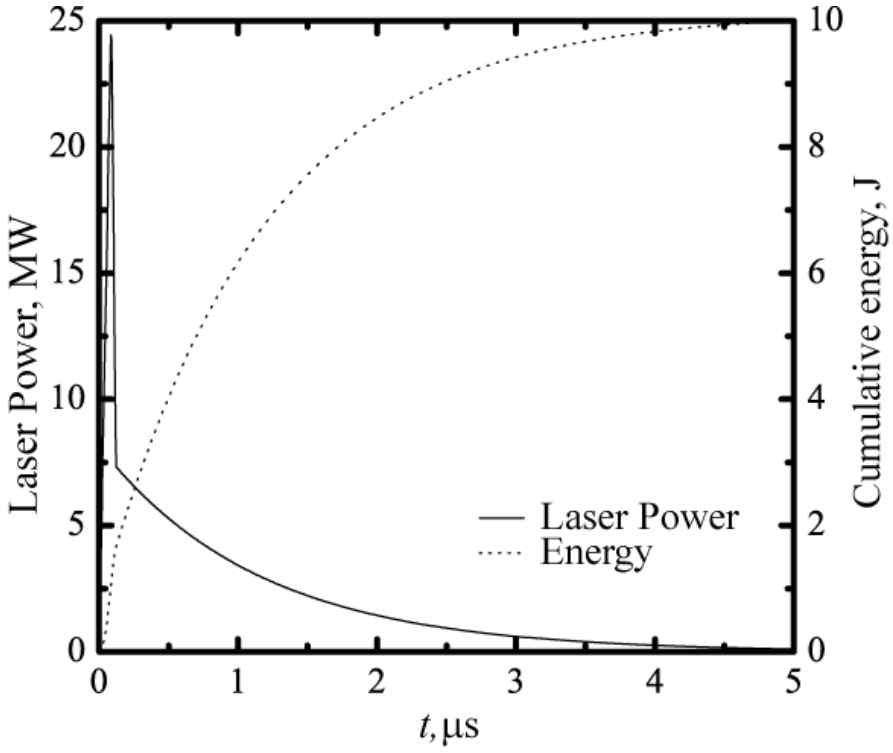

Figure 2.9 Pulse shape of CO_2 laser.

focussed onto an aluminium target plate in a chamber. Ablation was not observed on the surface of the target, and the experiments were carried out at 1 atm and under room-

temperature conditions. The schematic diagram of the CO_2 laser focusing setup for the respective effective diameters D, are shown in Figure 2.10.

2.2.2 Light Source, Imaging Apparatus and Experimental Setup

A diode pumped solid-state (DPSS) laser (continuous wave (CW), 532 nm, 1.45 W) was used as the probe light/ beam for the shadowgraph study of the induced discharge propagation. A spatial filter (with a 10 μm pinhole) was used to remove unwanted multiple-order energy peaks and spatial noise from the probe beam before traversing the test section. A pair of N-BK7 plano-convex spherical lenses with focal lengths of 500 mm and 300 mm respectively, were used to collimate the probe beam from the test section onto an imaging device. Images of the laser-induced plasma were taken using an Ultra 8 intensified charge coupled device (ICCD) camera, specifications of which are as shown in Table 2.3.

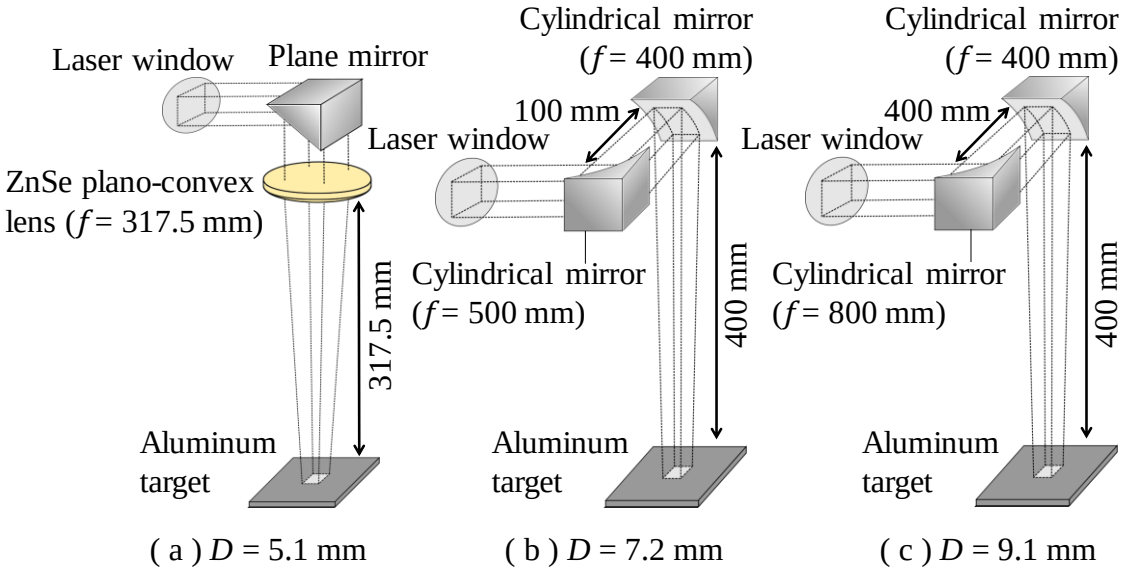

Figure 2.10 Schematic diagram of the focussing setup for the respective effective diameters.

Table 2.3 ICCD camera specification.

Product name	Ultra 8
Company	DRS Technology
Resolution	520 × 520 pixels per frame
Exposure time	> 10 ns
Camera sequence	Multiple
Frame per second	0.9

A pulse delay circuit/generator (Stanford Research Systems, Inc., Model №: DG535, rise time: 2 ns) was used to synchronize the operations of both the CO_2 laser and the ICCD camera, by receiving an electrical signal from the laser device and transmitting a transistor-transistor logic signal depending on the delay setting to the camera. The temporal and spatial resolutions of the experimental setup were 30 ns and 36 μm, respectively. Figure 2.11 shows the schematic diagram for the shadowgraph experiment setup in this study.

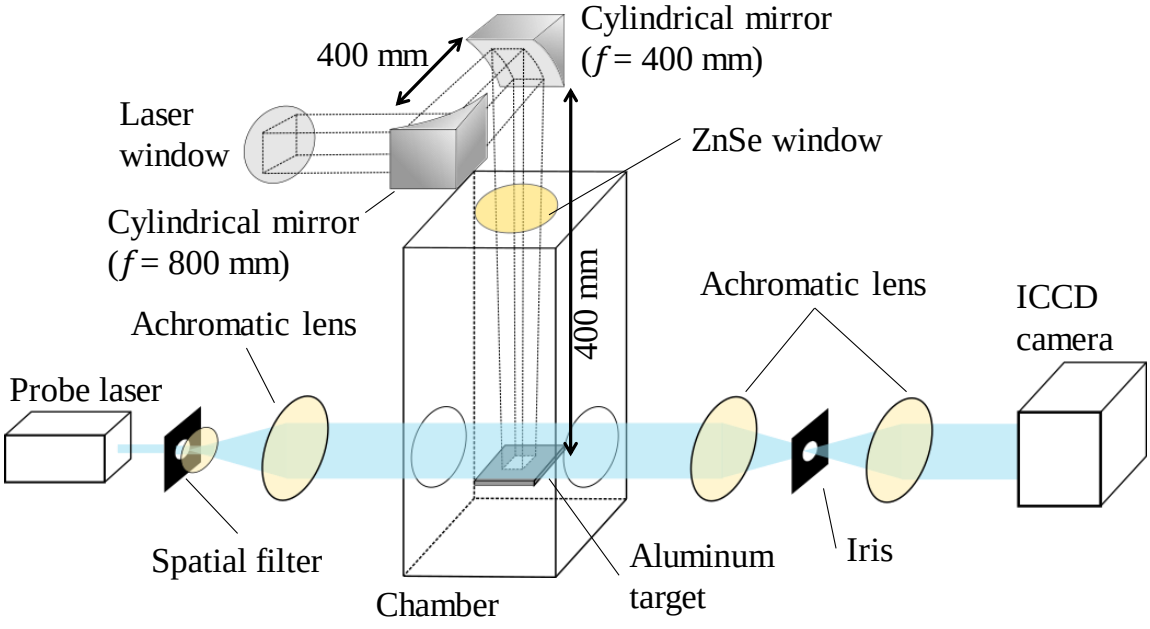

Figure 2.11 Schematic diagram of the shadowgraph experiment setup.

The laser beam quality factor for each spatial distribution is an important information necessary to design the focussing optics of the setup, in order to achieve the desired

effective diameters D. The beam quality factor for the Gaussian distribution M_{G}^2, and Top-hat distribution M_{T}^2, were estimated as 20 and 50 respectively. The effective diameter at the focus D, is defined as:

$$D = 2\sqrt{(D_{\mathrm{G}} D_{\mathrm{T}} / \pi)}\,. \tag{2.2}$$

Where D_{G} and D_{T} are respectively, the diameters at the focal point of the Gaussian and Top-hat distributions. These diameters are functions of the beam quality factor and their definition is given by Equation (2.3).[61]

$$D_{\mathrm{G,T}} = 2\frac{M_{\mathrm{G,T}}^2 \lambda f}{\pi \mathrm{R}}. \tag{2.3}$$

Here, λ is the laser wavelength, f is the focal length of the lens/mirror, and R is the pre-focused radius of the laser beam on the surface of the lens/mirror. The spatial intensity distributions for the case of $D = 7.2$ mm is shown in Figure 2.12. Approximately 86% of the laser beam power is confined within the area defined by D_{G} and D_{T}.

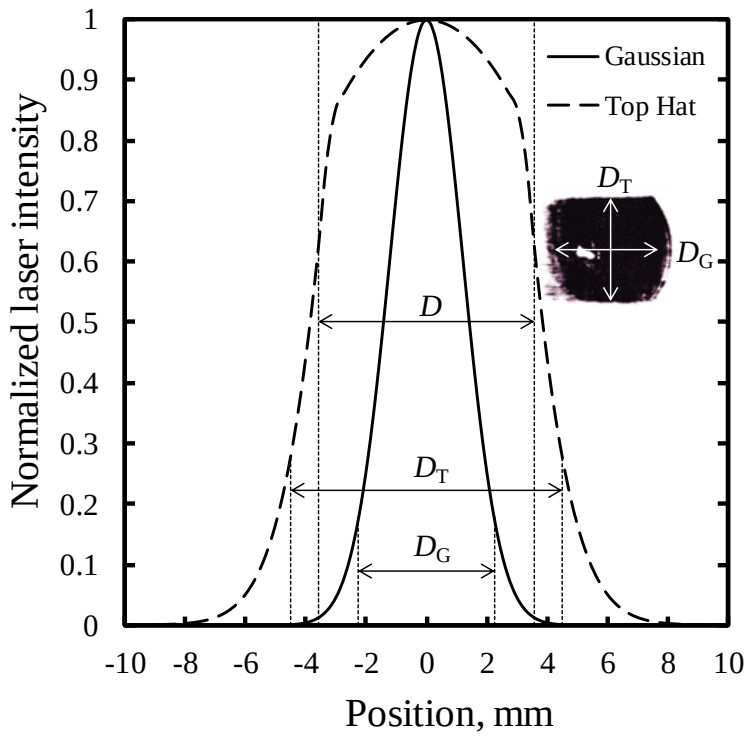

Figure 2.12 Spatial intensity distributions at the focus for the case D = 7.2 mm. Insert: Sample output burn pattern of CO_2 laser beam.

2.3 LID Extension Velocity Dependence on Beam Diameter and Gas Species[62]

Sample shadowgraph images of the propagation history (of the induced discharge) is shown in Figures 2.13 and 2.14 respectively for argon and helium gases. In the case of the argon gas, the laser beam D was 9.1 mm, whiles that of the helium gas was 5.1 mm. The wavefronts as indicated in the series of pictures are travelling in the opposite direction of the irradiated laser beam. The time t is the elapsed duration whose origin is defined as the initial irradiance of the laser beam. It is observed from the shadowgraph images that the induced discharge displacement was much extended in the helium gas as compared to that of the argon gas. Displacement-time ($x - t$) graphs are obtained from the shadowgraph images.

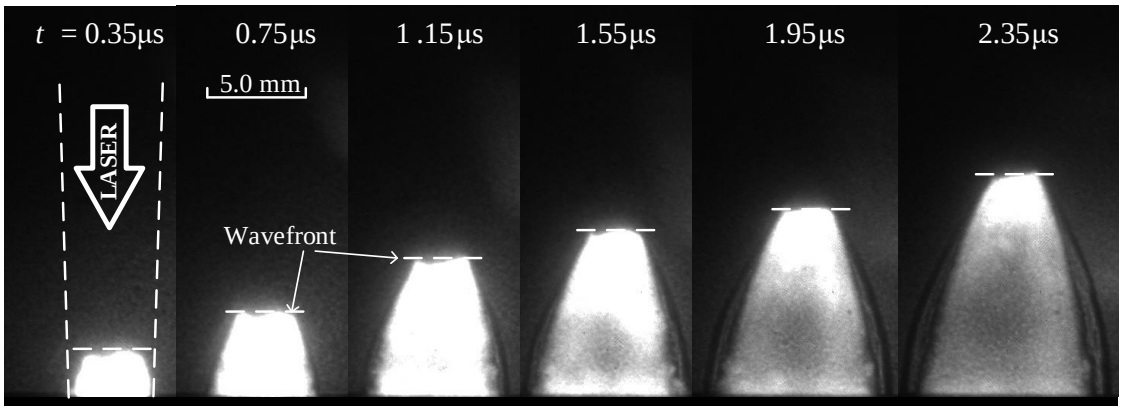

Figure 2.13 Shadowgraph images of LID in argon gas for the case D = 9.1 mm.

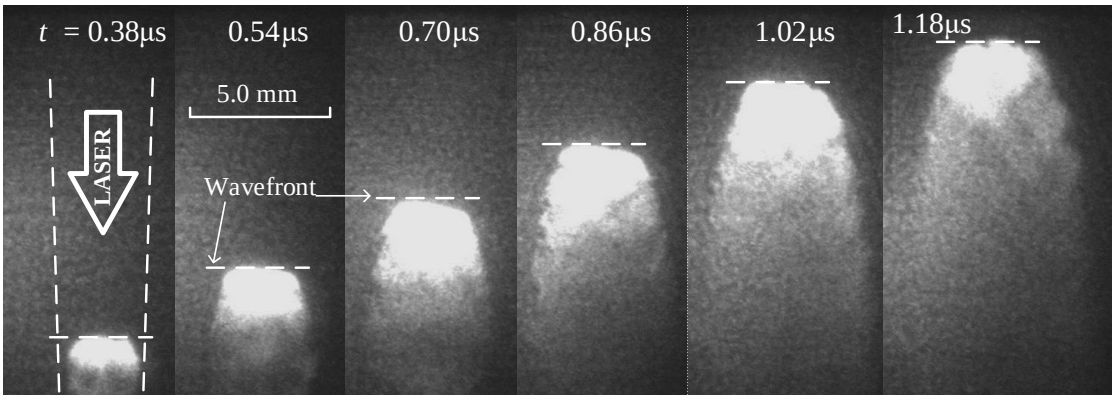

Figure 2.14 Shadowgraph images of LID in helium gas for the case D = 5.1 mm.

The extension velocity U_{LID}, was in turn analytically obtained from the $x-t$ graphs. An example of an $x-t$ graph and its corresponding $U_{\mathrm{LID}}-t$ for both argon and helium gases for the case of $D=7.2$ mm are shown in Figure 2.15. The displacement error bars are the standard error of the mean value. The velocity error bars were obtained by using the least squares method and they represent the propagated error as a result of deducing U_{LID} from x. Each data point represents the mean of five data points set.

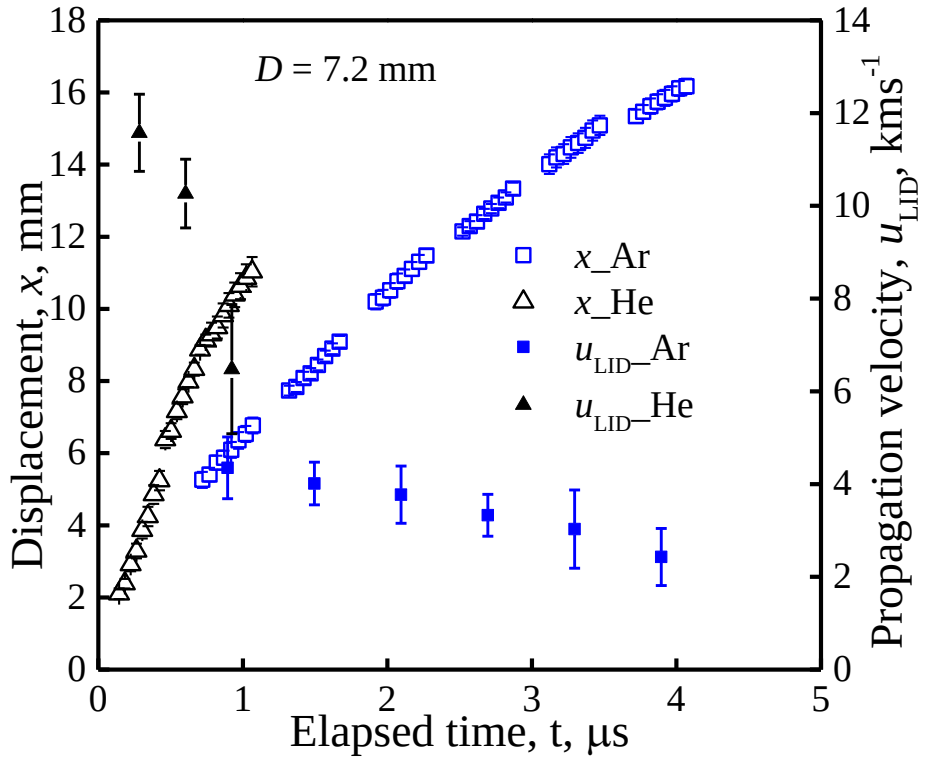

Figure 2.15 $x-t$ and $U_{\mathrm{LID}}-t$ plots in argon and helium gases for the case $D=7.2$ mm.

2.3.1 LID Extension Velocity Dependence on Beam Diameter

The dependence of the induced discharge extension (propagation) velocity on D is as shown in Figure 2.16. The essence of a sufficiently large D necessary to uniquely define U_{LID} as a function of S is demonstrated in this figure. The figure shows the velocities in argon gas for four different Ds. It is observed that for a D less than 7.2 mm, U_{LID} is slower for a given S and the dependence is not unique. Thus, a D of 7.2 mm was sufficient to

reproduce the experimental uniqueness for the relation $U_{\mathrm{LID}} \propto S^{\alpha}$. The propagation velocity is a localised phenomenon and thus the U_{LID} were graphed as function of the peak laser intensity S.

2.3.2 LID Extension Velocity Dependence on Gas Species

The dependence of the induced discharge extension velocity on gas species is as shown in Figure 2.17. The threshold value of D necessary to uniquely define $U_{\mathrm{LID}} \propto S^{\alpha}$ in helium gas was 5.1 mm. The exponential values of α for the relation $u_{\mathrm{LID}} \propto S^{\alpha}$, for helium, air and argon gases were respectively 1.18, 0.46 and 0.23. Table 2.4 shows the comparison of α values for studies with sufficiently large *D*s in the aforementioned gases.

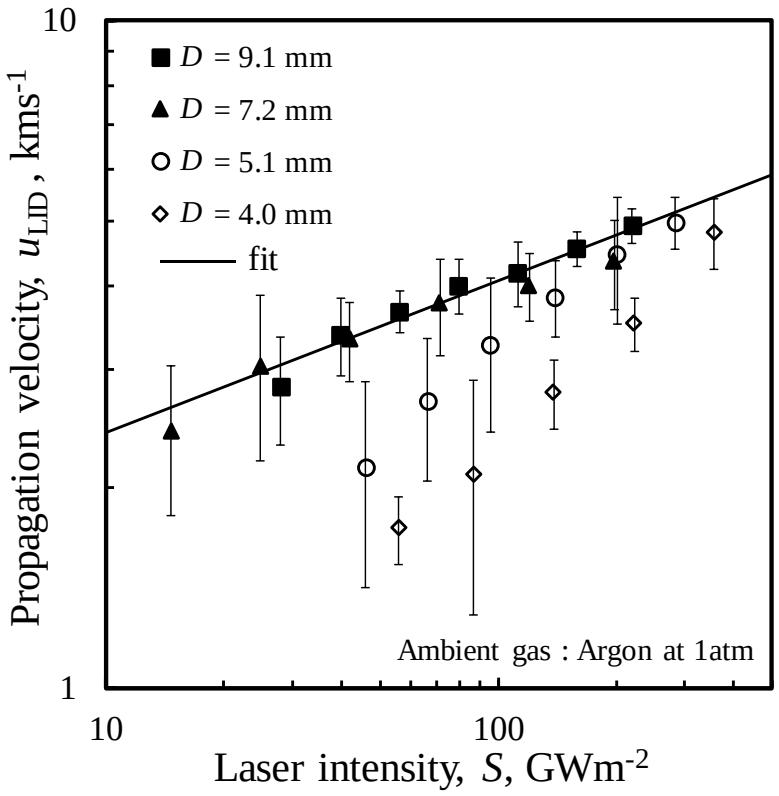

Figure 2.16 Propagation velocities as a function of S in argon for four different Ds.

Table 2.4 Comparison of α in Air, Argon and Helium gases with sufficiently large D.

Items	Gas species	α value
This Study	Argon	0.23
	Helium	1.18
	Air	0.46
Matsui *et al*[57]	Air	0.46
Bournot *et al*[51]		

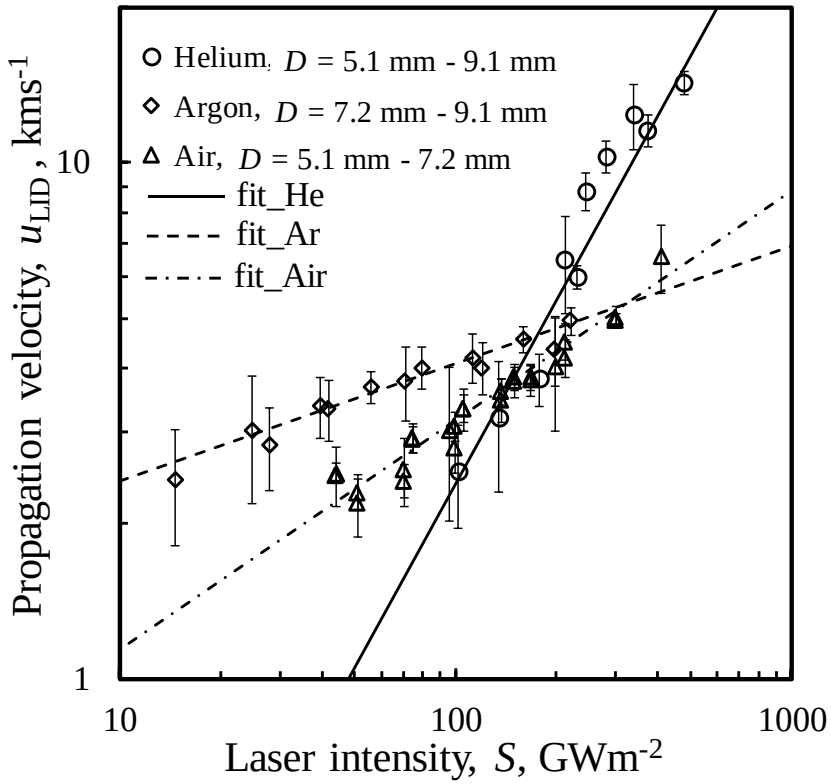

Figure 2.17 Propagation velocities as a function of S in different gases with sufficiently large Ds.

2.4 Summary

1. The threshold value of D necessary to uniquely define the relation $U_{\mathrm{LID}} \propto S^{\alpha}$ and to eliminate the effect of lateral dissipation was obtained for the three gases. This was 7.2 mm in all the gases studied. These values were sufficient to reproduce the experimental uniqueness for the relation $U_{\mathrm{LID}} \propto S^{\alpha}$. Further studies of the physics are necessary to investigate the universality of this criterion.

2. The values of the exponential parameter α in the relation $U_{\mathrm{LID}} \propto S^{\alpha}$ were 1.18, 0.46 and 0.23 respectively, for helium, air and argon gases.
3. The values of α obtained in this study for the three gases were different from the 0.33 value of the Chapman-Jouguet detonation theory. This corroborates the hypothesis that LID propagation is a discharge-based phenomenon and thus, U_{LID} should be determined from discharge-based physics and not fluid dynamics.
4. Observed differences in the α values in argon and helium will provide a key for understanding the physics of laser-induced discharge

CHAPTER 3

VALIDATION OF SHIMAMURA'S 1-D LID MODEL IN HELIUM AND ARGON GASES

3.1 Spectroscopic Measurement of T_{ex} and n_e

The first objective of this chapter was to predict the laser-induced discharge (LID) extension velocity U_{LID}, using Shimamura's 1-D LID photoionization model with experimentally obtained plasma properties (n_e, T_{ex}), of the induced discharge as input. The model equations (already defined in Equations (1.3) and (1.4)) are as shown in Equations (3.1) and (3.2).

$$U_{LID} = \frac{\nu_i l}{\ln\left(n_{e.peak}/n_{e.f}\right)}. \tag{3.1}$$

$$n_{e.f} = \frac{\phi}{U_{LID}}. \tag{3.2}$$

Where $n_{e.peak}$, $n_{e.f}$, ν_i, l and ϕ are respectively the peak and precursor electron number density, ionization frequency, inverse bremsstrahlung absorption length and the photon flux.

The 1-D LID model describes the precursor (seed) electrons as products of photoionization due to the flux coming from the induced discharge. The photon flux is a function of the bulk plasma properties, thus optical emission spectroscopic measurements were conducted in order to obtain the electronic excitation temperature T_{ex} of neutral particles, and the electron number density n_e, in the laser-induced discharge in both

helium and argon gases. The second objective was to validate the model by comparing analytically obtained results to that of experiment.

3.1.1 Experimental Setup

The schematic diagram of the optical emission spectroscopy setup is shown in Figure 3.1. The irradiation from the laser-induced discharge was collected with a fibre optic cable into the entrance slit of an Echelle spectrometer (ARYELLE 200, LTB) via an SMA port.

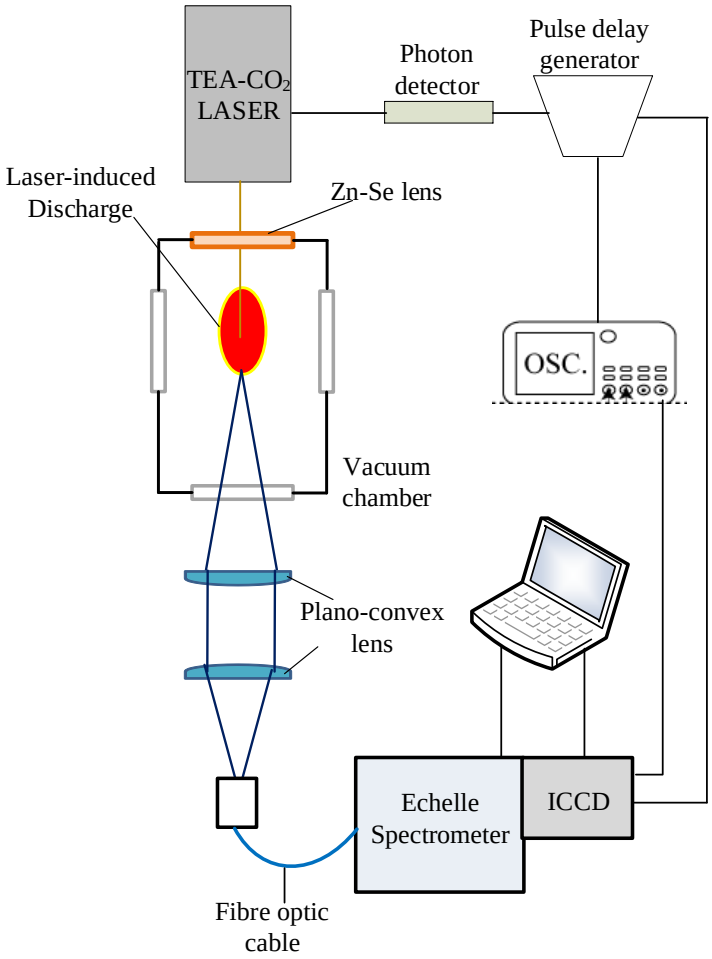

Figure 3.1 Schematic diagram of optical emission spectroscopy setup.

The spectrometer is coupled to an ICCD camera (iStar, Andor Technology), and the specifications of both devices are as shown in Table 3.1. The spectrometer shutter exposure time was 200 ns for the experiment. The experiments were carried out under standard atmospheric pressure and room temperature conditions.

Table 3.1 Spectrometer and ICCD camera specifications.

Spectrometer		ICCD camera	
Product name	ARYELLE 200	Product name	iStar
Company	Lasertechnik Berlin	Company	Andor Technology
Spectral resolving power ($\lambda/\Delta\lambda$)	8000	Resolution	1024 × 1024 pixels per frame
Wavelength range	330 – 850 nm	Exposure time	< 2 ns
Focal length	400 mm	Camera sequence	Single
Slit width	50 µm	Frames per second	Up to 100 million

3.1.2 Deduction of T_{ex} and n_e

Figures 3.2 and 3.3 show the emission spectra in helium and argon gases obtained respectively, in the range of 400 nm – 700 nm and 450 nm – 650 nm, at different laser intensities, S.

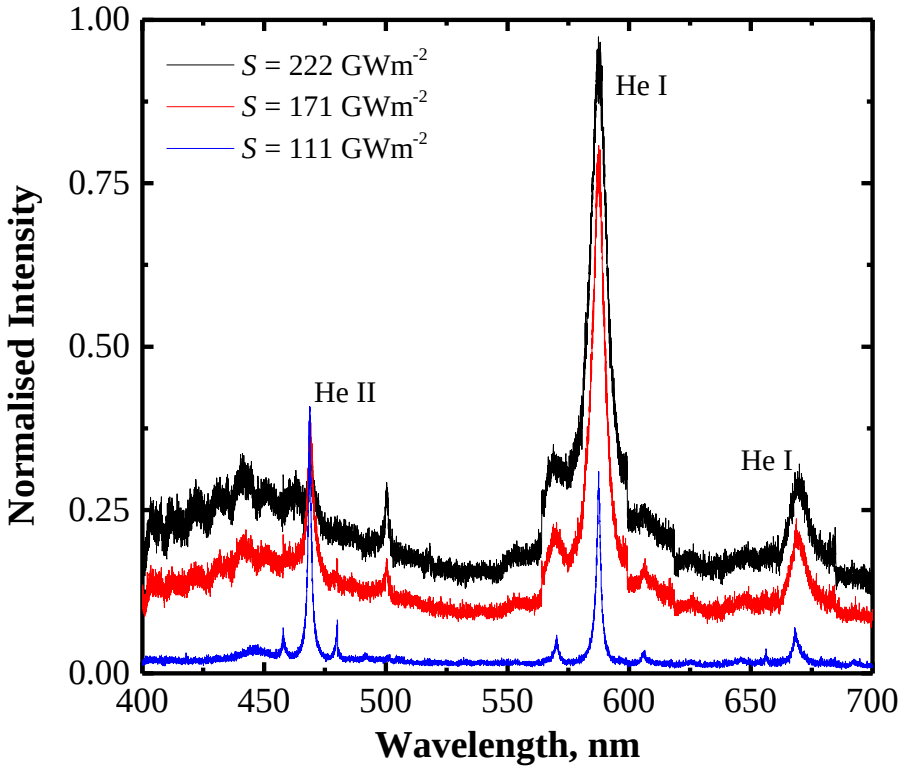

Figure 3.2 Sample observed spectra in helium. Intensity normalised by maximum value at $S = 222$ GWm^{-2}.

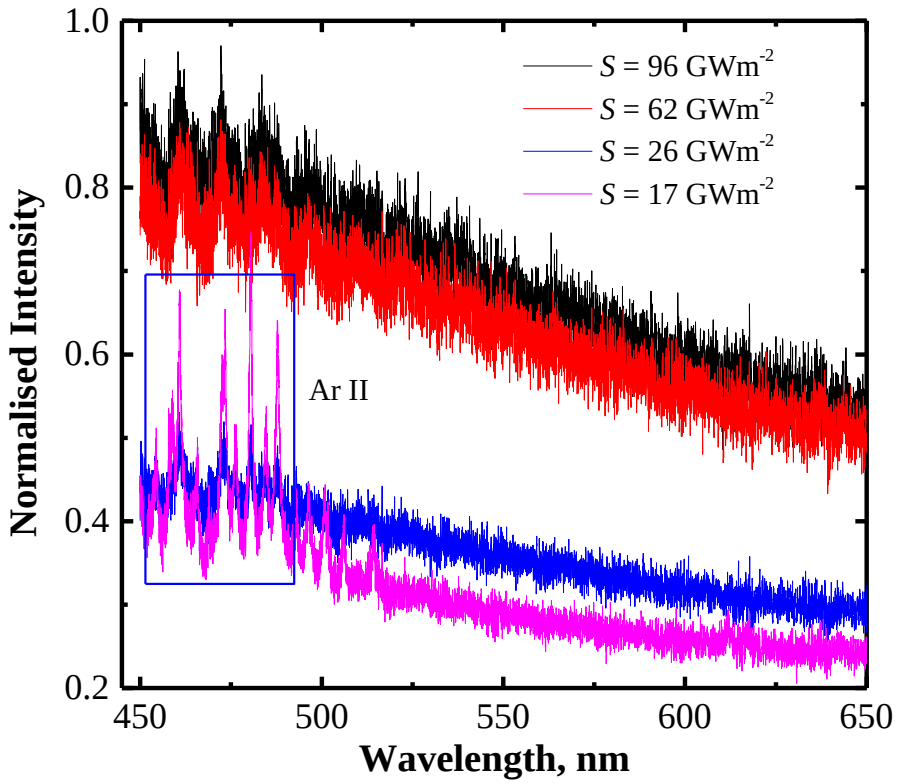

Figure 3.3 Sample observed spectra in argon. Intensity normalised by maximum value at $S = 96$ GWm^{-2}.

The spectral intensities are normalised by the maximum intensity in each graph. Line spectrum was not observed for the argon case except at $S = 17$ GWm^{-2}. In Figure 3.3, the continuum spectra contain information which is a superposition of both continuum and line spectra. Thus, the optical thickness for the induced discharge in argon gas was considered as neither thick (black-body radiation) nor thin (bremsstrahlung radiation). For the purpose of verifying this claim, the continuum spectra were fitted by both the black-body radiation function and bremsstrahlung (with free-bound transitions) radiation function.

The spectral intensity of black-body radiation per unit wavelength B_λ (Wm^{-3}), is as shown in Equation (3.3).[63]

$$B_\lambda = \frac{2\pi hc^2}{\lambda^5}\left[\exp\left(\frac{hc}{\lambda k_B T_{ex}}\right) - 1\right]^{-1} \tag{3.3}$$

Here, h, c, λ, k_{B} and T_{ex} are respectively the Planck constant, light speed in vacuum, wavelength, Boltzmann constant and the electron excitation temperature. The black-body radiation function fit, to the argon plasma continuum spectra at $S = 96$ GWm^{-2}, using Equation (3.3) is shown in Figure 3.4. The obtained excitation temperature from the fit was 0.65 eV, which is quite low and not representative of the experimental conditions of the LID by a 12 J CO_2 gas laser in our laboratory. A function fit of 2 eV shown on the graph deviates from the experiment condition.

The continuum spectra of argon were also fitted by bremsstrahlung radiation function (with free-bound transitions). The volumetric radiation per unit wavelength j_λ, was obtained from the volumetric radiation per unit frequency j_ν (Jm^{-3}),[63] noting that $j_\lambda = j_\nu(c/\lambda^2)$. This is as shown in Equation (3.4):

$$j_\lambda \mathrm{d}\lambda = \frac{64 Z_{\mathrm{eff}}^2 \pi^{3/2} e^6 G}{3\sqrt{6} m_{\mathrm{e}}^{3/2} c^2 \lambda^2 \varepsilon_0^3} \frac{n_{\mathrm{i}} n_{\mathrm{e}}}{\sqrt{k_{\mathrm{B}} T_{\mathrm{e}}}} \exp\left(\frac{-hc}{k_{\mathrm{B}} T_{\mathrm{e}}}\left(\frac{1}{\lambda} - \frac{1}{\lambda_{\mathrm{c}}}\right)\right) \mathrm{d}\lambda \qquad (3.4)$$

Here, Z_{eff}, e, G, m_{e} and ε_0, are respectively, the effective nuclear charge, the elementary charge, the Gaunt factor (for quantum-mechanical effect), the electron mass and the permittivity of free space. T_{e}, n_{i} and n_{e} are the electron temperature (defined as identical to T_{ex}), the ion and electron number densities respectively. λ is the wavelength and λ_{c} is the wavelength corresponding to the cut-off density for the input laser beam. n_{i} is set as n_{e} assuming quasi-neutrality condition in the induced discharge. G is defined in Equation (3.5) as:[64]

$$G = 1.04 + 3.74 \times 10^{-5} T_{\mathrm{e}} - 3.28 \times 10^{-10} {T_{\mathrm{e}}}^2 \qquad (3.5)$$

Figure 3.5 shows the bremsstrahlung radiation function fit at an electron excitation temperature T_{ex} of 3.5 eV to the spectra at S of 96 GWm^{-2}. This temperature value is high and not representative of the experimental conditions of the LID by a 12 J CO_2 gas laser in our laboratory. A function fit at 2 eV deviates from the experiment condition.

Thus, T_{ex} could not be derived from either black-body radiation fit or bremsstrahlung radiation fit to the argon plasma spectra. This validates the claim that, the LID in argon gas, was optically neither thick or thin. For future works, it is recommended that the induced plasma be sliced in order to obtain T_{ex} from spectra data for the case of the argon plasma.

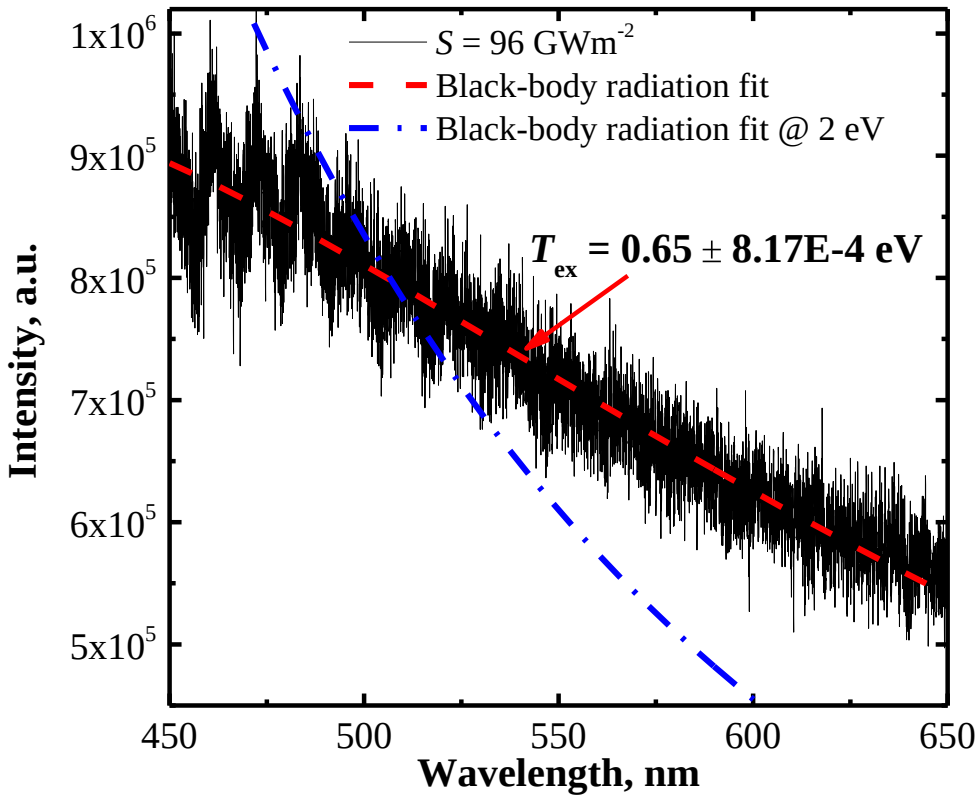

Figure 3.4 Black-body radiation function fit to argon spectra at $S = 96$ GWm^{-2}.

The line spectra obtained for the helium gas were not sufficient to deduce the electron temperature by the Boltzmann plot method. Thus, the electron number density n_e were first obtained from the Stark broadening parameters of He I line (587.6 nm), after which T_{ex} was deduced from the Saha ionization equation. For neutral atom lines, the relation between the Stark broadening width and n_e (cm^{-3}) is defined as:[65,67]

$$w_t(n_e, T_e) \cong 2w_e(T_e)[1 + gA_n(T_e)]n_e 10^{-16}. \quad (3.6)$$

Where w_t and w_e are respectively, the total theoretical full-width at half-maximum (FWHM) and the electron impact width. w_e was obtained from tables in Reference 66. g and A_n are respectively defined in Equations (3.7) and (3.8).[67]

$$g = 1.75(1 - 0.75R) \tag{3.7}$$

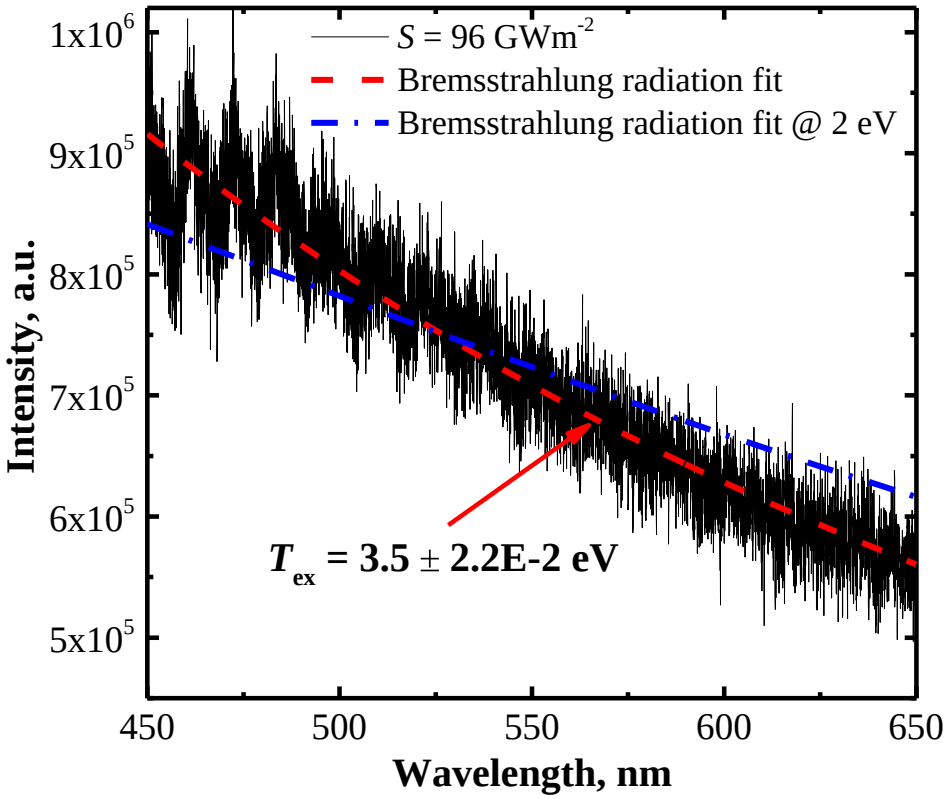

Figure 3.5 Bremsstrahlung radiation function fit to argon spectra at $S = 96$ GWm^{-2}.

Where R is the Debye shielding parameter and is defined as the ratio of the average inter-ion distance to the Debye radius.

$$A_n(T_e) = A(T_e){n_e}^{1/4}10^{-4} \tag{3.8}$$

Here A is the ion broadening parameter and is a measure of the distortion effect plasma fields have on broadened line widths or shifts. The applicability of Equation (3.6) require that the following restrictions (Equations (3.9) and (3.10)) be observed:[67]

$$R = 8.99 \times 10^{-2}{n_e}^{1/6}{T_e}^{-1/2} \leq 0.8 \tag{3.9}$$

$$0.05 \leq A_n(T_e) \leq 0.5 \tag{3.10}$$

For the CO_2 gas laser used in this study, parameter values (n_e, T_{ex}) of the order of (1×10^{24} m^{-3}, 2 eV), gives R and A_n as 0.59 and 0.215 respectively. $A(T_e)$ was referenced from tables in Reference 66 Based on these values, Equation (3.6) was approximated as:

$$w_t(n_e, T_e) \approx 2w_e(T_e)n_e 10^{-16}. \quad (3.11)$$

The w_t of the helium gas case at the intensities of 220 GWm^{-2}, 171 GWm^{-2} and 111 GWm^{-2} were respectively 8.70 nm, 5.99 nm and 1.97 nm. These widths were derived from the Lorentzian function fit to the experiment data.

The Saha ionization equation used to derive discharge properties from corresponding experimentally obtained properties is as shown in Equation (3.12).

$$\frac{{n_e}^2}{n_0} = \frac{g_e g_i}{g_0}\frac{(2\pi m_e k_B T_e)^{3/2}}{h^3}\exp\left(\frac{-\epsilon_i}{k_B T_e}\right). \quad (3.12)$$

Here, g_e, g_i, g_0 n_0 and ϵ_i are respectively the statistical weights of the electrons, ions, neutrals, the neutral number density and the ionization potential. In Equation (3.12), quasi-neutrality is assumed, thus $n_e = n_i$, the ion number density. The following first stage ionization equilibria, whose local thermodynamic equilibrium (LTE) conditions between ionization and recombination processes are defined by the Saha ionization equation was considered for the helium LID plasma:

$$\mathrm{He}[1S^2\ {}^1S_0] \Leftrightarrow \mathrm{He}^+\left[1S\ {}^2S_{1/2}\right] + e^- + 24.59\ \mathrm{eV}$$

The statistical weights obtained from the NIST database for each species were as follows:[68]

He I ($g_0 = 1$) and He II ($g_i = 2$).

3.2 Validation of the 1-D LID Model by Comparing Theoretical and Measured U_{LID} in Helium Plasma

The objective of this section was to theoretically predict the extension velocity U_{LID}, from the measured propagation properties (n_{e}, T_{ex}), of the induced discharge using the 1-D LID photoionization model. The applicability of the model is evaluated by comparing predicted solutions to that of experiment for the helium plasma case.

U_{LID} was analytically obtained as a function of the laser intensity S using the 1-D LID model equations (Equations 3.1 and 3.2). A simple minimization solution of U_{LID} as a function of the density at the precursor location $n_{\mathrm{e.f}}$, for the given input properties (n_{e}, T_{ex}) was obtained from the model equations. This is as described below in Equation (3.13), where $n_{\mathrm{e.peak}}$ is defined as n_{e}. Using the Newton's method, the minimization variable was solved for iteratively via Equation (3.14) until convergence was reached.

$$U_{\mathrm{LID}}(n_{\mathrm{e.f}}) = \frac{\nu_{\mathrm{i}} l(n_{\mathrm{e}}, T_{\mathrm{e}})}{\ln\left({}^{n_{\mathrm{e}}}/_{n_{\mathrm{e.f}}}\right)} - \frac{\phi(n_{\mathrm{e}}, T_{\mathrm{e}})}{n_{\mathrm{e.f}}} . \tag{3.13}$$

$$n_{\mathrm{e,f,i+1}} = n_{\mathrm{e,f,i}} - \frac{U_{\mathrm{LID}}\left(n_{\mathrm{e,f,i}}\right)}{\left[\frac{\mathrm{d}}{\mathrm{d}n_{\mathrm{e.f}}}\left(U_{\mathrm{LID}}\left(n_{\mathrm{e,f,i}}\right)\right)\right]} . \tag{3.14}$$

3.2.1 Ionization Frequency

The ionization frequency ν_{i}, is defined as shown in Equation (3.15).

$$\nu_{\mathrm{i}} = \frac{\alpha_{\mathrm{IB}} S}{e\epsilon_{\mathrm{i}}} . \tag{3.15}$$

Here, e, ϵ_{i} and α_{IB} are respectively, the elementary charge, ionization potential of the gas and the inverse bremsstrahlung absorption cross section. α_{IB} is the total cross section of the absorption mechanism due to both electron-neutral and electron-ion particles' interactions. The absorption cross section by a neutral particle within the vicinity of the electric field of a single electron is given in Equation (3.16).[69]

$$\alpha_{\mathrm{IB,en}} = \frac{e^2}{cm_{\mathrm{e}}\varepsilon_0}\frac{\nu_{\mathrm{m}}}{\omega^2 + {\nu_{\mathrm{m}}}^2} \ . \tag{3.16}$$

Here, ν_{m} and ω are the mechanical collision frequency and the laser frequency respectively. All other variables are as defined previously. Generally, $\omega \gg \nu_{\mathrm{m}}$ for most lasers, and thus Equation (3.16) is reduced to as shown in Equation (3.17).

$$\alpha_{\mathrm{IB,en}} \cong \frac{e^2}{cm_{\mathrm{e}}\varepsilon_0}\frac{\nu_{\mathrm{m}}}{\omega^2} \ . \tag{3.17}$$

For instance, the frequency of the CO_2 gas laser at a typical wavelength of 10.6 microns is 1.78×10^{14} s^{-1}. This is much greater than the ν_{m} of argon and helium gases which are respectively 4.0×10^{12} s^{-1} and 1.52×10^{12} s^{-1}. The electron-ion absorption cross section is as shown in Equation (3.18).[64,69]

$$\alpha_{\mathrm{IB,ei}} = 1.37 \times 10^{-27} G Z_{\mathrm{eff}}^2 \frac{\lambda^3}{\sqrt{T_{\mathrm{e}}}} n_{\mathrm{i}} \tag{3.18}$$

Here, λ and n_{i} are the laser wavelength and ion number density. n_{i} is set as n_{e} assuming quasi-neutrality condition in the induced discharge. G and Z_{eff}, are as previously defined.

3.2.2 Inverse Bremsstrahlung Absorption Length

The variable l was defined as the inverse bremsstrahlung (IB) absorption length l_{IB}. l_{IB} is the reciprocal of the IB absorption coefficient k_{IB}, which is the sum of both electron-ion and electron-neutral interactions. These are as defined in Equations (3.19) and (3.20) respectively.[64]

$$k_{\mathrm{IB,ei}} = \frac{4}{3}\left(\frac{2\pi}{3m_{\mathrm{e}}k_{\mathrm{B}}T_{\mathrm{e}}}\right)^{\frac{1}{2}} \frac{e^6\lambda^3}{hc^4 m_{\mathrm{e}}} n_{\mathrm{i}} n_{\mathrm{e}} \left[\exp\left(\frac{hc}{\lambda k_{\mathrm{B}}T_{\mathrm{e}}}\right) - 1\right]. \tag{3.19}$$

$$k_{\mathrm{IB,en}} = \frac{(k_{\mathrm{B}}T_{\mathrm{e}})^2 A(T_{\mathrm{e}})\lambda^3}{hc} n_{\mathrm{n}} n_{\mathrm{e}} \left[1 - \exp\left(\frac{hc}{\lambda k_{\mathrm{B}}T_{\mathrm{e}}}\right)\right]. \tag{3.20}$$

Here, k_B, h and $A(T_e)$ are the Boltzmann constant, the Planck constant and a temperature function for free-free transitions of electrons in the field of neutral particles. All other variables are as defined previously. The function $A(T_e)$ is defined in Equation (3.21).[70]

$$A(T_e) = 1.406 \times 10^{-6} T_e[\mathrm{K}]^{-7/2} \int_0^{\infty} \exp\left(\frac{-E}{T_e[\mathrm{eV}]}\right) E^2 Q(E) \mathrm{d}E \ . \qquad (3.21)$$

Here, E (eV) and Q (cm^2) are respectively, the energy and the total momentum transfer cross section. Q was obtained from the TRINITI database, which is accessible online from Reference 71.

3.2.3 Photon Flux

The photon flux ϕ was computed using Equation (3.22), which considers radiation propagating in a half solid angle.

$$\phi = \frac{2\pi}{\epsilon_i} \int_0^{\theta_0} J(x,\theta) \sin\theta \, \mathrm{d}\theta \ . \qquad (3.22)$$

Where, θ is the angle subtended by the incident photon's trajectory and the plane parallel to the direction of propagation of the induced discharge. This is schematically shown in Figure 3.6. $J(x,\theta)$ is the radiation intensity per unit solid angle (W.m^{-2}.sr^{-1}) and is as defined in Equation (3.23).[42]

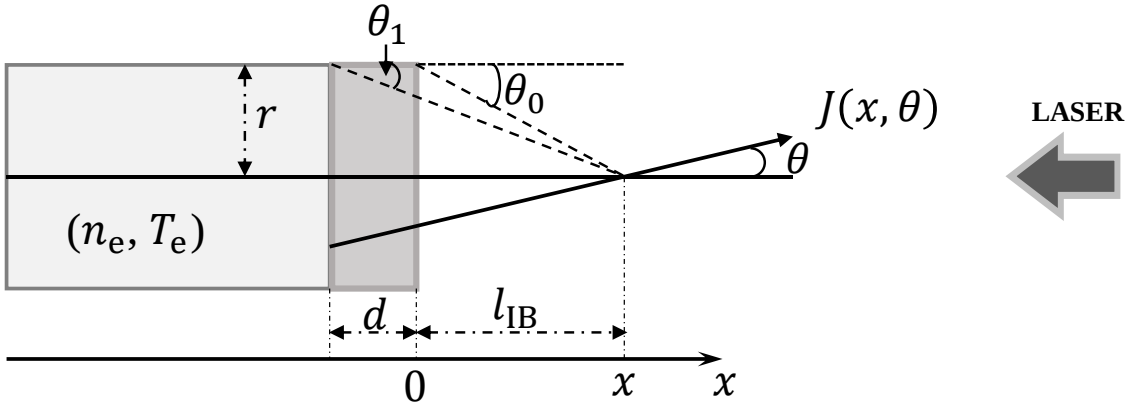

Figure 3.6 Schematic diagram showing photon flux estimation.

$$J(x,\theta) = \frac{j_i}{4\pi}\exp\left(\frac{-l_{\mathrm{IB}}}{\lambda_{\mathrm{mfp,pa}}\cos\theta}\right)\begin{cases}\dfrac{d}{\cos\theta}, & 0 < \theta < \theta_1\\ \dfrac{r}{\sin\theta} - \dfrac{l_{\mathrm{IB}}}{\cos\theta}, & \theta_1 < \theta < \theta_0\end{cases} \tag{3.23}$$

Where, j_i, $\lambda_{\mathrm{mfp,pa}}$, d and r are respectively, the total volumetric radiation density (Wm^{-3}), the mean-free path of photo-absorption, the thickness of the radiating layer and the radius of the radiating layer. r was set at 3 mm ($J(x,\theta)$ value is not changed for r ~ 3 mm – 5 mm), because a 7.2 mm effective diameter D has been experimentally demonstrated to suffice the threshold values in both argon and helium gases, required to uniquely define the discharge velocity as a function of laser intensity. d was set as 100 microns.

j_i was obtained by first integrating volumetric continuum radiations (free-free and free-bound emissions) over all frequencies starting from the ionization potential of the gas. The result was then multiplied by 2 in order to approximately account for line radiations (bound-bound emissions). This is as shown in Equation (3.24).[63]

$$j_i = 2\int_{\nu_{\mathrm{i}}}^{\infty}\frac{64Z_{\mathrm{eff}}^2\pi^{3/2}e^6G}{3\sqrt{6}m_{\mathrm{e}}^{3/2}c^3\varepsilon_0^3}\frac{n_{\mathrm{i}}n_{\mathrm{e}}}{\sqrt{k_{\mathrm{B}}T_{\mathrm{e}}}}\exp\left(\frac{-h(\nu_{\mathrm{i}}-\nu_{\mathrm{c}})}{k_{\mathrm{B}}T_{\mathrm{e}}}\right)\mathrm{d}\nu \tag{3.24}$$

Here, ν_{i} and ν_{c} are the frequencies corresponding to the ionization potential and cut-off density for the input laser energy. Incorporating Equations (3.15) – (3.24) into Equations (3.13) and (3.14), U_{LID} was obtained.

3.3 Results and Discussion

3.3.1 Measured n_{e} and Estimated T_{ex} of Helium Plasma

The experimentally obtained n_{e} and the estimated T_{ex} assuming Saha equilibrium for the helium gas, are shown Figure 3.7 as functions of the laser intensity S. n_{e} of the induced

discharge was in the range of 0.5 – 2.3×10^{24} m^{-3}, and T_{ex} was in the range of 1.7 – 2.0 eV.

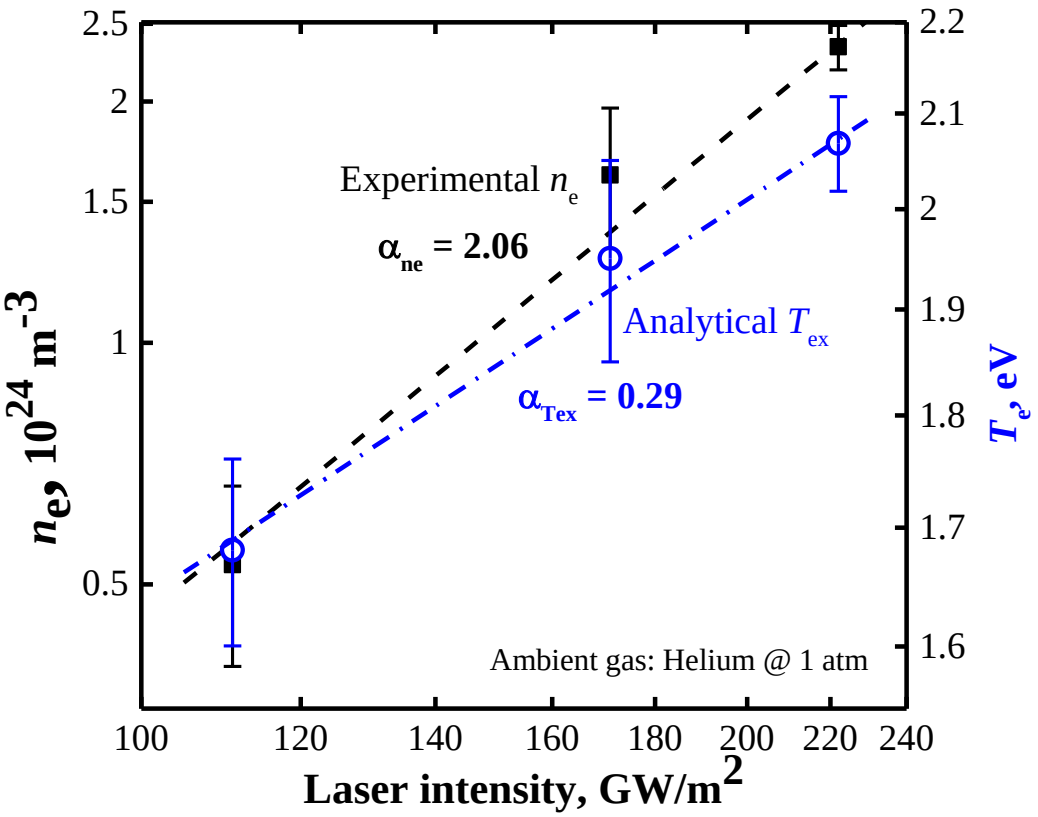

Figure 3.7 Experimental n_e and analytical T_{ex} as functions of laser intensity S for helium gas.

3.3.2 Comparison of Predicted and Measured U_{LID}

Figure 3.8 shows the comparison between theoretically predicted U_{LID}, using measured n_e and T_{ex}, and experimentally obtained U_{LID} trendlines for helium gas. The predicted U_{LID} showed very high value in the high intensity region when compared to the experimentally obtained U_{LID}. Moreover, the predicted exponential value (slope of the graph) α, was 1.83 compared to the 1.18 value from experiment.

Shimamura's 1-D LID model approximately reproduced the slope tendency of the relation $U_{LID} \propto S^{\alpha}$, however the absolute values of U_{LID} were overestimated. The

percent overestimation for the intensity range of 110 GWm^{-2} – 220 GWm^{-2} was 300% - 600%.

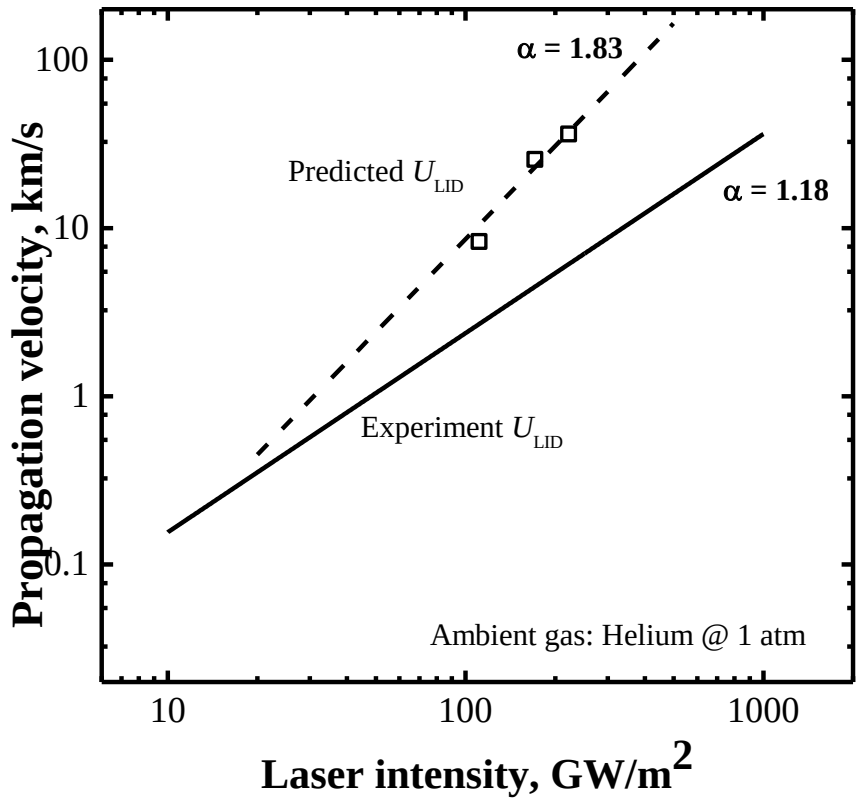

Figure 3.8 Predicted and measured velocities as a function of laser intensity in Helium plasma.

One of the possible explanations to the discrepancies between predicted and experimental extension velocities could be that, the 1-D LID model assumes a 100% utilization of the absorbed energy for direct ionization. The model does not take into account other energetic processes that could result in the excitation of particles without not necessarily inducing ionization. Information on the fraction of the absorbed energy used in ionization would be useful for improving the 1-D LID model.

3.4 Summary

1. Shimamura's 1-D LID model could reproduce the increasing slope tendency of the extension velocity as a function of the laser intensity in helium plasma. However, the absolute values of U_{LID}were 300% - 600% overestimated.
2. Comparisons were not made for the argon plasma because, obtained spectra were the superposition of continuum and line spectra observed in the experiments. Thus, it could not be classified as either an optically thin or thick plasma. In future studies, the induced plasma would be sliced in order to obtain T_{ex} from spectra data.

CHAPTER 4

FRACTIONAL ENERGY FOR IONIZATION AND TWO-STEP IONIZATION

4.1 Ionization Mechanism in Conventional CFD models

In a recent related study, the precursor generation and the laser absorption mechanism of the induced discharge was investigated numerically.[72] The study used a 1-D computational fluid dynamic (CFD) code which coupled the Navier-Stokes equations to a 3-temperature thermochemical non-equilibrium model. The Navier-Stokes equation took into consideration shock heating, electron diffusion and electron thermal conduction. The laser absorption process was modelled after the inverse bremsstrahlung absorption (IB) mechanism. The absorbed energy is stored in electrons' translational mode and the ionization is modelled via collisions with Maxwellian electrons.

The study could not reproduce the observed experimental criterion for sustaining the laser-supported detonation regime of LID. In other words, the shock heating and the IB absorption process for electron translational energy, could not generate sufficient ionization avalanche to replicate experimentally observed scenario. This is graphically shown in Figure 4.1. The failure was attributed to excessive electron recombination in the non-equilibrium region between shock front and the laser absorption front.

I am however of the view that, IB absorption process predominantly leads to the heating of electron and not necessarily the direct induction of ionization. Therefore, the IB absorption, together with the translation of electrons implemented in the computational

model would not be sufficient to reproduce the experiment conditions observed in laser-induced discharges.

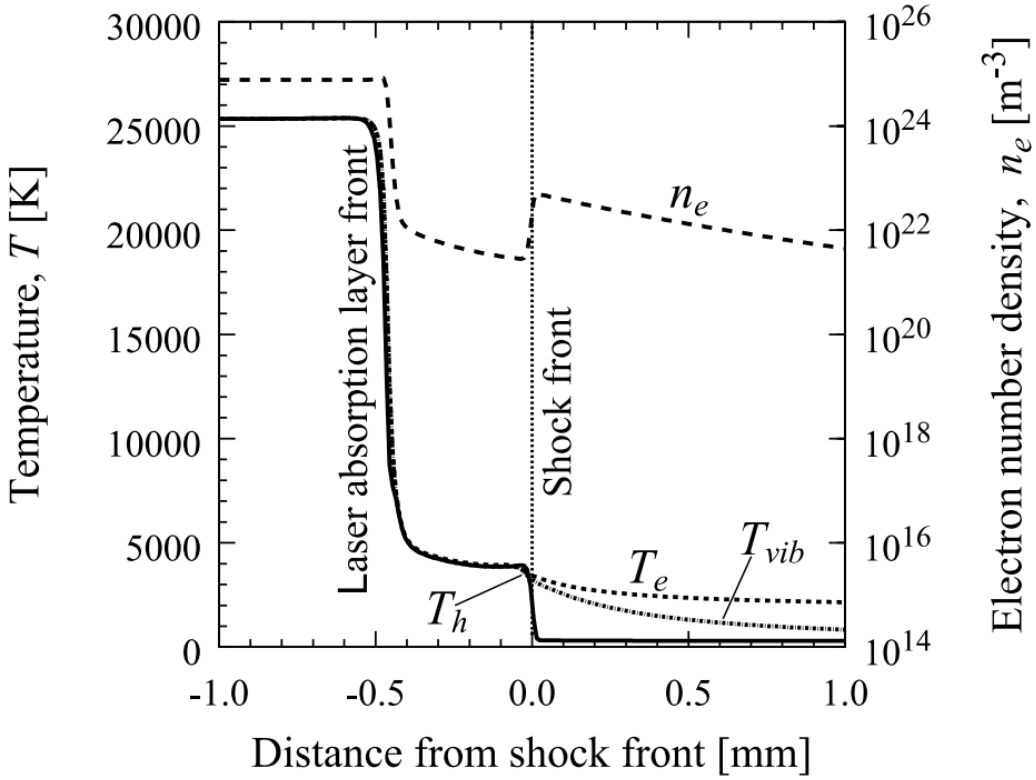

Figure 4.1 Density and temperature distributions of the 3-temperature model.[72]

4.2 Ionization Mechanisms of the Shimamura's Model

Shimamura's LID model describes the avalanche ionization stage via the inverse bremsstrahlung (IB) acceleration and/ or absorption process. The avalanche ionization process however, could be due to two different ionization mechanisms described as follows.

The first is the IB absorption process, which accelerates the photon-generated electrons to energy levels required to induce direct electron impact ionization. This acceleration process transfers energy to the electron by heating, which results in electron temperature increment. Thus, the electrons are heated to the required energy levels for impact

ionization. However, the fraction of energy that goes to heating of neutral particles is not considered in the model.

The second plausible description to the avalanche ionization is by a discharge mechanism, where seed electrons are accelerated by the electric field of the irradiated laser beam. This discharge mechanism, is also a function of the reduced electric field (E/n_{n}, E: electric field, n_{n}: density of neutral particles). This is pictorially shown in Figure 4.2. The discharge creates an avalanche ionization effect where, accelerated electrons collide with other particles leading to the ionization of the particles. The resulting free electrons are in turn accelerated and additional electrons generated to sustain the process in a sufficient electric field. However, in Shimamura's model, energy storage is not accounted for. In other words, absorbed energy is instantaneously consumed for ionization.

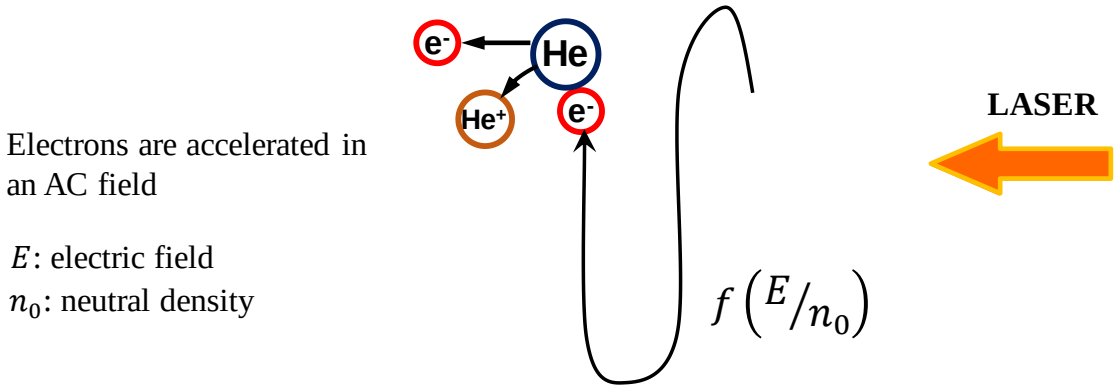

Figure 4.2 Collisions by field-accelerated electrons.

Presently, although Shimamura's LID model (a quasi-1D model) defines both the ionization frequency and absorption length as functions of the IB absorption process, the model however, could not reproduce the measured LID velocities U_{LID}. Thus, one possible way to improve the model would be to include coupled neutral particles' excitation and collisions with field – accelerated electrons as proposed in the next section.

4.3 Cumulative (Two-Step) Ionization Mechanisms

In Chapter 3, the predicted extension velocity U_{LID} of the induced discharge was not representative of the experimentally obtained velocities for the helium plasma. The model's representation of the discharge velocity in actual 1-D beam propagation was inaccurate. The 1-D LID model assumes that all the absorbed energy is directly utilized for ionization. It is therefore necessary to obtain the fraction of the absorbed energy used in ionizing the ambient working gas from experimentally obtained U_{LID} and laser intensity S.

4.3.1 Fractional Absorbed Energy for Ionization

The change in enthalpy/ laser heating (amount of absorbed energy) Δh (J/kg), as a function of the input laser intensity S, is given in Equation (4.1).

$$\Delta h = \frac{S}{\rho U_{\mathrm{LID}}} . \tag{4.1}$$

Where ρ is the density of the gas.

Figure 4.3 shows Δh as a function of S for both argon and helium gases. The Δh for argon plasma had a positive slope, whiles that of helium plasma was negative.

The amount of absorbed energy E_{i} (J/kg), utilized for ionizing the electron number density n_{e}, is given in Equation (4.2).

$$E_{\mathrm{i}} = \frac{\epsilon_{\mathrm{i}}\, n_{\mathrm{e}}}{\rho} . \tag{4.2}$$

Where ϵ_{i} is the ionization potential of the gas. Thus, the fraction of absorbed energy that is utilised for ionization η_{Ei}, was estimated as the ratios of Equations (4.2) and (4.1), and is as shown in Equation (4.3).

$$\eta_{\mathrm{Ei}} = \frac{\epsilon_{\mathrm{i}}\, n_{\mathrm{e}}}{S/U_{\mathrm{LID}}} . \tag{4.3}$$

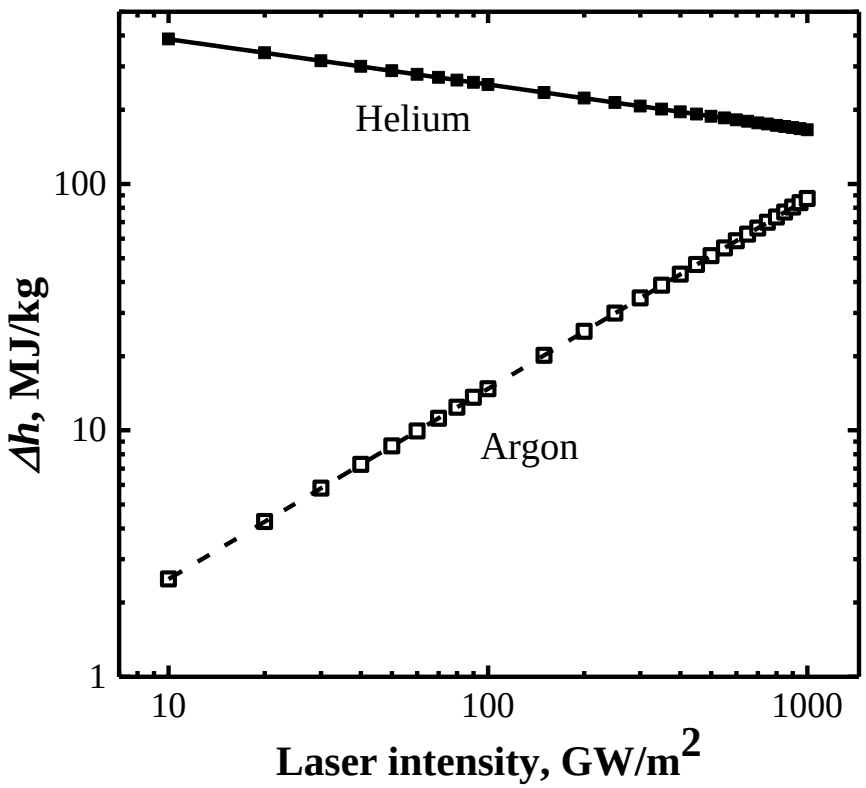

Figure 4.3 Change in enthalpy as a function of laser intensity in argon and helium plasmas.

Figure 4.4 shows the absorbed energy Δh, the energy used for ionization E_{i} and the energy difference ΔE ($\Delta E \equiv \Delta h - E_{\mathrm{i}}$), as functions of the later intensity S, for the helium plasma. Here, it is assumed that the absorbed energy is utilized for energetic interactions predominantly leading to excitation of neutral particles and their subsequent ionization by inelastic collisions with electrons accelerated by the laser field. This assumption is justified by the obtained values of E_{i} (which is much less than the ionization potential of the gas). This is because, excited particles would usually require lower ionization energies than those at the ground state. Figure 4.5 also shows the fraction of the absorbed energy utilized for ionization η_{Ei}, as well as the difference in fractions $\Delta\eta$ ($\Delta\eta \equiv 1 - \eta_{\mathrm{Ei}}$). The deduced η_{Ei} (in percent values) as a function of the laser intensity S, for the LID helium plasma was within the range of 5% - 25%. These obtained values contradict the

100% direct utilisation of absorbed energy for ionization, assumed in Shimamura's 1-D LID model.

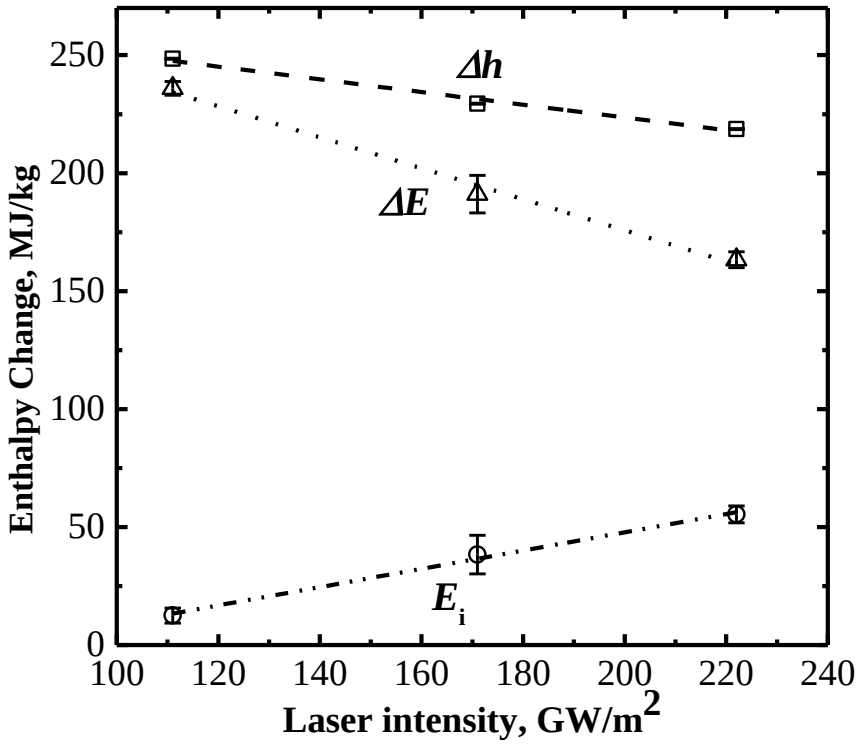

Figure 4.4 Absorbed energy, ionization energy and energy difference, as functions of laser intensity in helium gas.

4.3.2 Two-step Ionization Process

The ionization mechanism is a cumulative one (two-step ionization), where particles are first excited, and then ionized. This is because, the examined laser intensity was far below the breakdown threshold or critical intensity for the occurrence of induced discharge. Thus, neutral particles must be preheated by excitation collisions, making the two-step ionization process the most prevalent case when compared with direct ionization from ground state of particles. It is observed from Figures 4.4 and 4.5 that for the lower intensity condition, higher excitation energy (preheating) is necessary to sustain the laser-induced discharge and its propagation. Thus, the two-step ionization process is significant in the low intensity region.

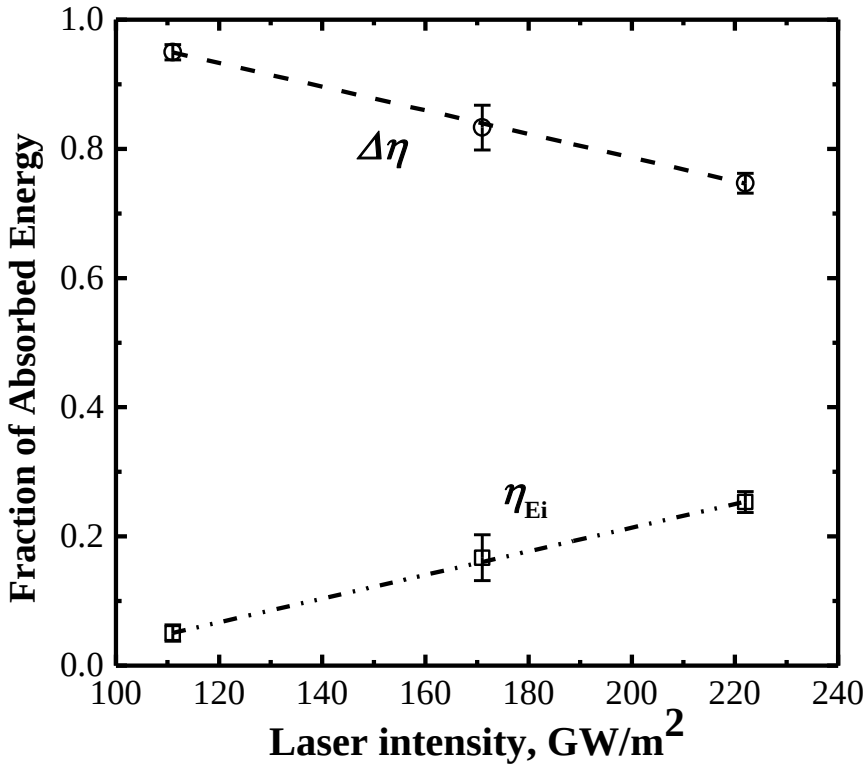

Figure 4.5 Fraction of absorbed energy used for energetic interactions and ionization as functions of laser intensity in helium gas.

Shimamura's LID model was successful in reproducing the extension velocity in previous experiments in argon gas.[43] This is because, the previous experiments were conducted with an effective laser beam diameter *D* of 2 mm. Thus, the approach of direct ionization from the ground state reproduced experimental condition. However, this approach for *D*s of 5 mm and above, failed to reproduce the experimentally obtained extension velocity U_{LID}.

In order to accurately predict the LID extension velocity in sufficiently large effective beam diameter situations (1-D beam propagation conditions), the following recommendations are made based on the outcome of this study. The 1-D LID model must include the two-step ionization process, as well as the appropriate fraction of absorbed energy used for excitation (heating of neutral particles) and ionization. The avalanche

ionization process of the LID propagation should be implemented by the collisions of excited neutrals with field-accelerated electrons, where fraction of absorbed energy is first stored in the excitation mode of neutral particles. The comparison of the three discussed discharge propagation models are shown in Table 4.1.

Table 4. 1 Comparison of LID discharge propagation models.

Mechanism	Katsurayama CFD model	Shimamura's LID model	Ofosu's proposal
Absorption	Inverse Bremsstrahlung absorption	Inverse Bremsstrahlung absorption	Inverse Bremsstrahlung absorption
Energy storage	Electron translational mode	-	Neutral excitation mode
Ionization	Collisions with Maxwellian electrons	Collisions by field-accelerated electrons	Collisions of excited neutrals with field-accelerated electrons

4.4 Summary

1. The amount of absorbed energy used for ionization was obtained to be 5% - 25% as a function of intensity for the LID helium plasma. This contradicts the 100% utilisation of absorbed energy for ionization in the Shimamura's 1-D LID model.
2. 5% - 25% values of the absorbed energy represent 2% - 9% of the ionization potential of helium gas. Thus, ionization occur from excited states of atom rather than from ground state.
3. The 1-D LID model successfully reproduced the experimental extension velocity in argon gas for a *D* of 2 mm, but was unable to reproduce experiment conditions for *D*s of 5 mm and above.
4. Higher excitation energies are necessary to sustain the induced discharge, especially in the low intensity region. Therefore, the two-step ionization process accounting for fractions of absorbed energy should be incorporated in to the 1-D

LID model. This involves energy storage in neutral particles' excitation mode and subsequent ionization via collisions of excited neutrals with field-accelerated electrons.

CHAPTER 5

CONCLUSION

The aim of this study was to characterise the extension velocities of laser-induced discharge in various gases, specifically in argon and helium gases.

First, it was experimentally demonstrated that sufficiently large effective beam diameters *D*, is required to uniquely define the relation between the extension velocity and laser intensity: $U_{\mathrm{LID}} \propto S^{\alpha}$. The D sufficiently large to uniquely define the relation $U_{\mathrm{LID}} \propto S^{\alpha}$ and to eliminate lateral dissipation of energy was 7.2 mm in all the gases studied. The value of the exponential parameter α, was gas dependent and was 1.18. 0.46 and 0.23 respectively, in helium, air and argon gases. The obtained α values were different from the 0.33 value of the Chapman-Jouguet detonation theory. This validates the hypothesis that U_{LID} is a discharge-based phenomenon and must be determined from discharge-based physics and not from fluid dynamics. The observed differences in the α values would be a key to understanding the physics of laser-induced discharge.

Second, it was observed that because Shimamura's 1-D LID model assumes 100% utilization of absorbed energy for ionization, the model could approximate the tendency of the slope for the relation $U_{\mathrm{LID}} \propto S^{\alpha}$ obtained from experiment. However, the model overestimated the absolute values of the extension velocity U_{LID}, in helium plasma by 300% - 600% within the intensity range of 110 $\mathrm{GWm^{-2}}$ – 220 $\mathrm{GWm^{-2}}$. Thus, the model should be improved by incorporating an energy conservation scheme.

Third, observing that ionization could be predominantly an accumulated process of various energetic interactions and not necessarily from the ground state of atoms directly,

it was demonstrated from the experiment that, higher excitation energies are required to sustain the induced discharge especially in the low intensity region.

Finally, based on the outcome of this work, it is recommended that, the two-step ionization process (first excitation, then ionization) should be implemented in the model, taking into account the fractions of absorbed energy required for each step. This involves energy storage in neutral particles' excitation mode and subsequent ionization via collisions of excited neutrals with field-accelerated electrons.

References

1. Wertz, J., and Larson, W.: *Reducing Space Mission Cost*, Kluwer Academic Publishers, Boston, 1996.
2. Space Freighter, http://cannae.com/space-freighter/ (accessed December 6, 2017).
3. Reusability: The key to making human life multi-planetary, http://www.spacex.com/news/2013/03/31/reusability-key-making-human-life-multi-planetary (accessed December 5, 2017).
4. SpaceX's new price chart illustrates performance cost of reusability, http://spacenews.com/spacexs-new-price-chart-illustrates-performance-cost-of-reusability/ (accessed December 5, 2017).
5. Berning, P.R., Hummer, C. R., and Hollandsworth, C. E.: A coilgun-based launch system, *IEEE Transactions on Magnetics*, **35**, 1, pp. 136-141.
6. Parker, J. V.: Electromagnetic projectile acceleration utilizing distributed energy sources, *Journal of Applied Physics*, **53,** 10 (1982), 6710.
7. Sanger, E.: "Zur Theorie der Photonenraketen," in Probleme der Weltraumforschang, 4th International Astronautical Congress, Zurich, 1953.
8. Shad, J.L. and Moriarty, J.J.: Microwave Rocket Concept, in 16th International Astronautical Congress, Athens, 1965.
9. Kantrowitz, A.: Propulsion to Orbit by Ground-Based Lasers, *Astronautics & Aeronautics*, **10** (1972), pp. 74-76.
10. Minovich, M. A.: Reactorless Nuclear Propulsion – The Laser Rocket, AIAA paper 72-1095, *AIAA/SAE 8th Joint Propulsion Specialist Conference*, December 1972.

11. Komurasaki, K., and Wang, B.: Laser Propulsion. in Encyclopedia of Aerospace Engineering, (2010), R. Blockley and W. Shyy (eds). John Wiley & Sons Ltd, Chichester, UK, pp. 1351-1360.
12. Bae, Y.: Photonic Laser Propulsion: Proof-of-Concept Demonstration, J. Spacecraft and Rockets, **45**, 1 (2008), pp. 153-155.
13. Myrabo, L. N.: "Highways of Light", *The Future of Space Exploration* by Scientific American, 1999, pp.66-67.
14. Phipps, C.R., Luke, J.R., Helgeson W., and Johnson, R.: Performance Test Results for the Laser-Powered Microthruster, *Beamed Energy Propulsion: Fourth International Symposium on Beamed Energy Propulsion,* AIP Conference Proceedings, **830**, (2006), pp. 224-234.
15. Toyoda, K., Komurasaki, K., and Arakawa, Y.: Thrust Performance of a CW Laser Thruster in Vacuum, *Vacuum*, **65**, (2002), pp. 383-388.
16. Sasoh, A., Jeung, I.S., and Choi, J.Y.: Access to Space without Energy and Propellant on Board, *Beamed Energy Propulsion: Fifth International Symposium on Beamed Energy Propulsion*, AIP Conference Proceedings, **997** (2007), pp. 37- 46.
17. Frisbee, R. H., Horvath, J. C. and Sercel, J. C.: Laser Propulsion for the Orbital Transfer Mission, *AIAA Paper*, 85-1224 1985.
18. Resendes, D. P., Mota, S., Mendonca, J. T., Sanders, B., Encarnacao, J., and Gonzalez del Amo, J.: Laser Propulsion for Ground Launch, *Journal of Propulsion and Power*, **23**, (2007), pp. 73-80.
19. Myrabo, L. N., Messitt, D. G., and Mead Jr., F. B.: Ground and Flight Tests of a Laser Propelled Vehicle, *AIAA Paper*, 98-1001, Reno 1998.
20. Katsurayama, H., Ushio, M., Komurasaki, K., and Arakawa, Y.: Feasibility for the Orbital Launch by Pulse Laser Propulsion, *Journal of Space Technology and Science*, **20**, 2 (2005), pp. 32-42.
21. Brandstein, A. and Levy, Y.: "Laser Propulsion System for Space Vehicles, *J. Prop. Power*, **14**, 2, (1998), pp. 261-269.
22. Raizer, Y.P.: Breakdown and Heating of Gases Under the Influence of a Laser Beam, *Soviet*

Physics Uspekhi, **8**, 5 (1966), pp. 650-673.

23. Ushio, M., Komurasaki, K., Kawamura, K. and Arakawa, Y.: Effect of laser supported detonation wave confinement on termination conditions, *Shock Waves*, **18** (2008), pp. 35-39.
24. Lee, John H. S.: *The Detonation Phenomenon*, Cambridge University Press, New York, 2008, pp. 6, 39-51, 65-71, 73-75.
25. Zeldovich, Y. B.: Theory of detonation, *Journal of Experimental and Theoretical Physics* (USSR), **10** (1940), pp. 542 – 568.
26. Von Neumann, J.: Theory of Detonation Waves, Report No. 549, Office of Science Research and Development, Washington, DC (1942), pp. 1-34.
27. Doring, W.: Detonation waves. *Ann. Phys. 5e Folge*, **43** (1943), pp. 421 – 436.
28. Zhang, F. (ed.): *Shock Wave Science and Technology Reference Library: Detonation Dynamics*, Springer-Verlag Berlin Heidelberg, **6** (2012), pp. 33 – 100.
29. Raizer, Y.P.: *Laser-induced discharge phenomenon*, Studies in Soviet Science, Consultants Bureau, New York, 1977, pp. 199-206.
30. Shimamura, K.: Ionization kinetics in a laser-supported detonation wave and its propagation limits, *PhD Graduation Thesis*, The University of Tokyo, March 2014, pp. 18-19.
31. Mori, K., Komurasaki, K., and Arakawa, Y.: Influence of the focusing f number on the heating regime transition in laser absorption waves, *J. Appl. Phys.*, **92** (2002), pp. 5663-5667.
32. Mori, K., Komurasaki, K., and Arakawa, Y.: Energy transfer from a laser pulse to a blast wave in reduced-pressure air atmospheres, *J. Appl. Phys.*, **95** (2004), pp. 5979-5983.
33. Mori, K., Komurasaki, K., and Arakawa, Y.: Threshold laser power density for regime transition of a laser absorption wave in a reduced-density air atmosphere, *Appl. Phys. Lett.*, **88** (2006), pp. 121502-1-121502-3.
34. Shimamura, K., Hatai, K., Kawamura, K., Fukui, A., Fukuda, A., Wang, B., Yamaguchi, T., Komurasaki, K. and Arakawa, Y.: Internal structure of laser supported detonation waves by two-wavelength Mach-Zehnder interferometer, *J. Appl. Phys.*, **109**, 084910 (2011), pp. 1-7.
35. Raizer, Y. P.: *Gas Discharge Physics*, Springer, New York, 1991.

36. Kulikovsky, A. A.: The role of the absorption length of photoionizing radiation in streamer dynamics in weak fields: a characteristic scale of ionization domain, *J. Phys. D: Appl. Phys.*, **33** (2000), pp. L5-L7.
37. Koopman, D. W.: Precursor ionization fronts ahead of expanding laser-plasmas, *Physics of Fluids*, **15**, 1 (1972), pp. 56-&.
38. Diziere, A., *et al.*: Highly radiative shock experiments driven by GEKKO XII, *Astro. Space Sci.*, **336**, 1 (2011), pp. 213-218.
39. Shimamura, K., Ofosu, J. A., Komurasaki, K., and Koizumi, H.: Predicting propagation limits of laser-supported detonation by Hugoniot analysis, *Jpn. J. Appl. Phys.*, **54**, 016201 (2015), pp. 1-5.
40. Ramsden, S. A. and Savic, P.: A radiative detonation model for the development of a laser-induced spark in air, *NATURE*, **203**, 4951 (1964), pp. 1217 – 1219.
41. Taylor, G.: The formation of a blast wave by a very intense explosion. I. Theoretical Discussion, *Proc. Roy. Soc.*, **201**, 1065 (1950), pp. 159-174.
42. Raizer, Y. P.: Heating of a gas by a powerful light pulse, *Soviet Physics J. Exptl. Theoret. Phys.*, **21** (1965), pp. 1009-1017.
43. Shimamura, K. Komurasaki, K., Ofosu, J. A., and Koizumi, H.: Precursor ionization and propagation velocity of a laser-absorption wave in 1.053 and 10.6 μm wavelengths laser radiation, *IEEE Trans. Plasma Sci.*, **42** (2014), pp. 3121-3128.
44. Itikawa, Y.: Cross Sections for Electron Collisions with Oxygen Molecules, *J. Phys. Chem. Ref. Data*, **38**, 1 (2009), pp. 1-20.
45. Itikawa, Y.: Cross Sections for Electron Collisions with Nitrogen Molecules, *J. Phys. Chem. Ref. Data*, **35**, 31 (2006), pp. 1-23.
46. Fisher, V. I.: Fast gas-ionization wave in a high-power laser beam, *Sov. Phys. JETP*, **52**, 6 (1980), pp. 1083-1088.
47. Ono, R., and Oda, T.: Visualization of Streamer Channels and Shock Waves Generated by Positive Pulsed Corona Discharge Using Laser Schlieren Method, *Jpn. J. Appl. Phys.*, **43**, 1 (2004), pp. 321-327.

48. Hoffert, M. I., and Lien, H.: Quasi-One-Dimensional, Nonequilibrium Gas Dynamics of Partially Ionized Two-Temperature Argon, *Physics of Fluids*, **10** (1967), pp. 1769-1777.
49. Ofosu, J. A.: Influence of the ambient gas content on the propagation properties of laser supported detonation wave: A case study on Argon and Nitrogen gases, *Master's Graduation Thesis*, The University of Tokyo, March 2014, p. 47.
50. Maher, W. E., Hall, R. B., Johnson, R. R.: Experimental study of ignition and propagation of laser-supported detonation waves, *J. Appl. Phys.*, **45** (1974), pp. 2138-2145.
51. Bournot, P., Pincosy, P. A., Inglesakis, G., Autric, M., Dufresne, D., and Caressa, J.-P.: Propagation of a laser-supported detonation wave, *Acta Astronautica*, **6** (1979), pp. 257-267.
52. Bufetov, I. A., Prokhorov, A. M., Fedorov, V.B., and Fomin, V.K.: Optical discharge accompanying a restriction imposed on lateral expansion of gas and a reduction in the threshold of light-induced detonation, *J. Exptl. Theoret. Phys. Lett.*, **39** (1984), pp. 258-260.
53. Gal'burt, V. A., and Ryabov, O. A.: Transient phenomena during supersonic propagation of an optical breakdown in gases, *Sov. J. Quantum Electron*, **18** (2008), pp. 1379-1384.
54. Ilyin, A. A., Nagorny, I. G., and Bukin, O. A.: Supersonic regimes of plasma expansion during optical breakdown in air, *Appl. Phys. Lett.*, **96**, 171501 (2010), pp. 1-2.
55. Boiko, V. A., Danilychev, V. A., Duvanov, B. N., Zvorykin, V. D., and Kholin, I. V.: Observation of supersonic radiation waves in gases generated by CO_2 laser radiation, *Sov. J. Quantum Electron*, **8** (1978), pp. 134-135.
56. Zakharchenko, S. V.: Superdetonation optical discharge waves in air (λ=1.06μ), *Sov. J. Quantum Electron*, **14** (1984), pp. 1429.
57. Matsui, K., Shimano, T., Ofosu, J. A., Komurasaki, K., Schoenherr, T., and Koizumi, H.: Accurate propagation velocity measurement of laser supported detonation waves, *Vacuum*, **136** (2017), pp.171–176.
58. Mori, K.: Energy conversion processes in air-breathing pulse-laser propulsion, *PhD Graduation Thesis*, The University of Tokyo, March 2003, pp. 23 – 27.
59. Poehler, T. O., and Walker, R. E.: Chemical lasers, *APL Technical Digest*, March – April, 1972, pp. 2 – 10.

60. Smith, D. C., and DeMaria, A. J.: Parametric Behavior of the Atmospheric Pressure Pulsed CO_2 Laser, *J. Appl. Phys.*, **41** (1970), pp. 5212 – 5214.
61. Svelto, O.: *Principles of Lasers, 5 ed.*, Springer Science+Business Media, New York, 2010, pp. 157. 222, 492.
62. Shimano, T., Ofosu, J. A., Matsui, K., Komurasaki, K., and Koizumi, H.: Laser-induced discharge propagation velocity in helium and argon gases, *Trans. Japan Soc. Aero. Space Sci.*, **60**, 6 (2017), pp. 371-378.
63. Bose, T. K.: *High Temperature Gas Dynamics, An Introduction for Physicists and Engineers, 2 ed.*, Springer International Publishing, Switzerland, 2014, pp. 99-102.
64. Kemp, N. H., and Lewis, P. F.: *Laser – Heated Thruster - Interim Report*, NASA Contractor Report, NASA CR-161665, 1980, pp. 11-21.
65. Griem, H. R.: *Spectral Line Broadening by Plasmas*, Academic Press, New York, 1974.
66. Griem, H. R.: *Plasma Spectroscopy*, McGraw-Hill, New York, 1964.
67. Konjevic, N.: Plasma Broadening and Shifting of Non-hydrogenic Spectral Lines: Present status and applications, *Physics Reports*, **316** (1999), pp. 339-401.
68. (Online). NIST Atomic Spectra Database, https://www.nist.gov/pml/atomic-spectra-database.
69. Zeldovich, Y. B., and Raizer, Y. P.: *Physics of Shock Waves and High-Temperature Hydrodynamic Phenomenon*, Courier Corporation, 2002, pp. 259-260, 282-285.
70. John, T. L.: The free-free Transitions of Atomic and Molecular Negative Ions in the Infrared, *Mon. Not. R. astr. Soc.*, **170** (1975), pp. 5-6.
71. (Online). TRINITI database, www.lxcat.net/TRINITI.
72. Katsurayama, H., Mishima, K., and Katoh, Y.: A 1-D Numerical Analysis of a Laser Supported Detonation with Multiple Thermal Non-equilibrium and Precursor Radiation Heating, 2017-b-31, *31st International Symposium on Space Technology and Science*, Ehime, Japan, June 2017.

List of Academic Publications

Journal Publications

1) K. Shimamura, K. Matsui, **J. A. Ofosu**, I. Yokota, and K. Komurasaki,: Mode transition of plasma expansion for laser induced breakdown in Air, *Appl. Phys. Lett.*, **110** (2017), 134104. (http://dx.doi.org/10.1063/1.4979646)
2) T. Shimano, **J. A. Ofosu**, K. Matsui, K. Komurasaki, and H. Koizumi,: Laser-induced discharge propagation velocity in helium and argon gases, *Trans. Japan Soc. Aero. Space Sci.*, 60, 6 (2017), pp. 371 – 378. (https://doi.org/10.2322/tjsass.60.378)
3) K. Matsui, T. Shimano, **J. A. Ofosu**, K. Komurasaki, T. Schoenherr, and H. Koizumi,: Accurate propagation velocity measurement of laser supported detonation waves, *Vacuum*, **136**, (2017), pp. 171 - 176. (http://dx.doi.org/10.1016/j.vacuum.2016.07.011)
4) K. Shimamura, **J. A. Ofosu**, K. Komurasaki, and H. Koizumi,: Predicting propagation limits of laser-supported detonation by Hugoniot analysis, *Jpn. J. Appl. Phys.*, **54**, (2015), 016201. (http://dx.doi.org/10.7567/JJAP.54.016201)
5) K. Shimamura, K. Komurasaki, **J. A. Ofosu**, and H. Koizumi,: Precursor ionization and propagation velocity of a laser-absorption wave in 1.053 and 10.6 μm wavelengths laser radiation, *IEEE Trans. Plasma Sci.*, **42** (2014), pp. 3121 – 3128. (http://dx.doi.org/10.1109/TPS.2014.2304960)

Conference Proceedings and Presentations

International

1) ○**J. A. Ofosu**, R. Kawashima, K. Matsui, T. Shimano, K. Komurasaki, K. Shimamura, and H. Koizumi,: Internal structure of LSD wave based on a 1-D laser-induced discharge model: comparison between numerical simulation and experiment, *AVIATION 2016/ 47th AIAA Plasmadynamics & Lasers Conference,* Washington, D.C., USA, June 13 – 17, 2016.
2) R. Kawashima, **J. A. Ofosu**, K. Matsui, T. Shimano, K. Komurasaki, K. Shimamura, and H. Koizumi,: Numerical Investigation of LSD Wave Characteristics Using a 1-D Laser-induced Discharge Model, *International High Power Laser Ablation and Directed Energy Symposia*, Santa Fe, New Mexico, USA, April 4 – 7, 2016.
3) K. Matsui, **J. A. Ofosu**, T. Shimano, K. Komurasaki, K. Shimamura, and H. Koizumi,: Laser Intensity and LSD Wave Propagation Velocity in a Large Diameter Beam, *International High Power Laser Ablation and Directed Energy Symposia*, Santa Fe, New Mexico, USA, April 4 – 7, 2016.
4) K. Matsui, T. Shimano, **J. A. Ofosu**, K. Komurasaki, T. Schoenherr, and H. Koizumi,: Laser-supported detonation generated in a laser beam of 7 mm diameter, *The 10th International Symposium on Applied Plasma Science*, Nara, Japan, August, 2015.
5) ○**J. A. Ofosu**, K. Matsui, K. Komurasaki, K. Shimamura, and H. Koizumi,: Simulation of LSD wave characteristics in Ar and N_2 using a 1-D laser-induced discharge model coupled with hydrodynamic relations for laser-propelled thruster studies, *Joint Conference of 30th International Symposium on Space Technology and Science, 34th International Electric Propulsion Conference and 6th Nano-satellite Symposium*, Hyogo-Kobe, Japan, July 4 – 10, 2015.

6) K. Matsui, **J. A. Ofosu**, K. Shimamura, K. Komurasaki, and H. Koizumi,: The effect of intensity profile on LSD wave propagation velocity and its application to laser propulsion system, *Joint Conference of 30th International Symposium on Space Technology and Science, 34th International Electric Propulsion Conference and 6th Nano-satellite Symposium*, Hyogo-Kobe, Japan, July 4 – 10, 2015. (Poster Presentation)

7) ○**J. A. Ofosu**, K. Shimamura, K. Komurasaki, and H. Koizumi,: Structural profiling of laser-absorption layer in a laser-produced plasma of different gas media using 2-wavelength Mach-Zehnder interferometry, *International High Power Laser Ablation and Beamed Energy Propulsion Symposia*, Santa Fe, New Mexico, USA, April 21-25, 2014.

8) K. Shimamura, ○**J. A. Ofosu**, M. Fukunari, and K. Komurasaki,: One-dimensional control volume analysis and limit of laser-supported detonation for high propulsive efficiency, *International High Power Laser Ablation and Beamed Energy Propulsion Symposia*, Santa Fe, New Mexico, USA, April 21-25, 2014. (Poster Presentation)

9) K. Shimamura, **J. A. Ofosu**, K. Komurasaki, and H. Koizumi,: Effect of ionization waves on propagation of a laser-supported detonation wave, *45th AIAA Plasmadynamics and Lasers Conference, AIAA Aviation and Aeronautics Forum and Exposition*, Atlanta, Georgia, USA, PDL-01, June 16-20, 2014.

10) ○**J. A. Ofosu**,: Characterization of Laser-supported detonation density profile using two-wavelength Mach-Zehnder Interferometer, *29th International Symposium on Space Technology and Science*, Nagoya, Japan, 2013-s-62-b, June 3-7, 2013.

11) K. Shimamura, **J. A. Ofosu**, and K. Komurasaki,: Influence of the self uv-radiation on the structure of the laser-supported detonation wave, *29th International*

Symposium on Space Technology and Science, Nagoya, Japan, 2013-b-25, June 3-7, 2013.

12) K. Shimamura, **J. A. Ofosu**, M. Fukunari, and K. Komurasaki,: A weak-overdriven detonation mode for laser-produced plasma, P3-39, *IEEE Pulsed Power & Plasma Science*, San Francisco, California, USA, 2013.

13) K. Shimamura, **J. A. Ofosu**, M. Fukunari, H. Koizumi, and K. Komurasaki,: Radiation structure of laser-produced plasma at low mach-number by 2-wavelength Mach-zehnder interferometer, P3-36, *IEEE Pulsed Power & Plasma Science*, San Francisco, California, USA, 2013.

14) K. Shimamura, K. Michigami, **J. A. Ofosu**, and K. Komurasaki,: Influence of the gaseous form on the precursor heating layer of a laser supported detonation wave using half self-emission half shadowgraph visualization, DPP12-2012-000069, *54th Annual Meeting of the APS Division of Plasma Physics*, Rhode island, USA, 2012. [Abstract and PPT]

Domestic

1) 松井康平，島野徹，**J. A. Ofosu**，小紫公也，小泉宏之，“一次元的なレーザー支持デトネーションにおける電離波面速度とレーザー強度の関係”，航空宇宙学会第47期年会講講演会，東京，2016年4月.
2) 松井康平，**J. A. Ofosu**，島野徹，嶋村耕平，小紫公也，小泉宏之，“7 mmの集光系を用いたレーザー支持デトネーションの伝播特性”第 59 回宇宙科学技術連合講演会，鹿児島，2015年10月.（ポスター）
3) **J. A. Ofosu**，〇松井康平，嶋村耕平，小紫公也，小泉宏之，“Determination of LSD wave velocity in Ar and N_2 by a laser induced discharge model with deionization process and measured parameters”，第58回宇宙科学技術連合講演会，長崎，2014年11月.

4) 松井康平，**J. A. Ofosu**，小紫公也，小泉宏之，嶋村耕平，“高エネルギーパルスレーザーの応用とLSD伝播に及ぼす影響”，第58回宇宙科学技術連合講演会，長崎，2014年11月.

5) ○**J. A. Ofosu**, K. Shimamura, K. Komurasaki, and H. Koizumi,: Prediction of LSD wave velocity in Argon and Nitrogen using a 1-D radiative hydrodynamic model and measured parameters, *45th Annual General Meeting/ Lecture of the Japan Society for Aeronautical and Space Sciences*, Tokyo, Japan, April 10-11, 2014.

6) ○**J. A. Ofosu**, K. Shimamura, K. Komurasaki, and H. Koizumi,: 2 Dimensional electron density profiling of plasma by interferometry and fringe pattern analysis, *JAXA Institute of Space and Astronautical Science' (ISAS) Space Transportation symposium*, Sagamihara, Kanagawa, Japan, STEP-2013-069, January 16-17, 2014.

7) ○**J. A. Ofosu**, K. Shimamura, K. Komurasaki, and H. Koizumi,: Experimental investigations of laser supported detonation properties in a CO_2 laser-produced plasma, *57th Japan Society for Aeronautical and Space Sciences Conference*, Yonago, Tottori, Japan, 1I05, October 09-11, 2013.

8) 嶋村耕平、**J. A. Ofosu**, 小紫公也 自己輻射がレーザーデトネーションの伝播に与える影響 平成24年度衝撃波シンポジウム, 1A1-4, 小倉, 2013年3月（口頭発表)

9) 嶋村耕平、**J. A. Ofosu**, 小紫公也 レーザーデトネーションの自己輻射がその伝搬に与える影響 第53回航空原動機・宇宙推進講演会, JSASS-2013-0032, 倉敷, 2013年3月（口頭発表)

10) 嶋村耕平、**J. A. Ofosu**, 小紫公也 レーザーデトネーションにおける自己輻射と先駆電離層に関する考察, 平成２４年度宇宙輸送シンポジウム, STEP-2012-017, 相模原, 2013年1月（口頭発表)

11) ○**J. A. Ofosu**, K. Shimamura, K. Komurasaki, and H. Koizumi, Y. Arakawa,: Influence of gas type on internal structure of laser supported detonation using 2-wavelength Mach-Zehnder interferometer, *56th Japan Society for Aeronautical and Space Sciences Conference*, Beppu, Oita, Japan, 3J19, November 20-22, 2012.

12) 嶋村耕平、**J. A. Ofosu**, 小紫公也 レーザーデトネーションの伝播構造に関する実験的研究 日本航空宇宙学会第44期年会講演会, A13, 本郷, 2012年4月（口頭発表)

Award

2014 HPLA/ BEP Conference 2nd Place Poster award

Title: "One-dimensional control volume analysis and limit of laser-supported detonation for high propulsive efficiency"

Authors: K. Shimamura, **J.A. Ofosu**, M. Fukunari and K. Komurasaki

Note

○: Represents/ indicates the presenter.